

Lattice Boltzmann-Based Approaches for Pore-Scale Reactive Transport

Hongkyu Yoon

*Geoscience Research and Applications
Sandia National Laboratories
Albuquerque, New Mexico 87185, USA
hyoon@sandia.gov*

Qinjun Kang

*Earth and Environmental Sciences Division
Los Alamos National Laboratory
Los Alamos, New Mexico 87545, USA*

Albert J. Valocchi

*Department of Civil and Environmental Engineering
University of Illinois at Urbana-Champaign
Urbana, Illinois 61801, USA*

INTRODUCTION

Important geoscience and environmental applications such as geologic carbon storage, environmental remediation, and unconventional oil and gas recovery are best understood in the context of reactive flow and multicomponent transport in the subsurface environment. The coupling of chemical and microbiological reactions with hydrological and mechanical processes can lead to complex behaviors across an enormous range of spatial and temporal scales. These coupled responses are also strongly influenced by the heterogeneity and anisotropy of the geologic formations. Reactive transport processes can change the pore morphology at the pore scale, thereby leading to nonlinear interactions with advective and diffusive transport, which can strongly influence larger-scale properties such as permeability and dispersion. Therefore, one of the greatest research challenges is to improve our ability to predict these processes across scales (DOE 2007). The development of pore-scale experimental and modeling methods to study reactive processes involving mineral precipitation and dissolution, and biofilm dynamics allows more fundamental investigation of physical behavior so that more accurate and robust upscaled constitutive models can be developed for the continuum scale.

A pore-scale model provides fundamental mechanistic explanations of how biogeochemical processes and pore-scale interfacial reactions alter flow paths by pore plugging (and dissolving) under different geochemical compositions and pore configurations. For example, dissolved CO₂ during geological CO₂ storage may react with minerals in fractured rocks, confined aquifers, or faults, resulting in cementation (and/or dissolution) and altering hydrodynamics of reactive flow. This can be observed in a natural analogue where primary porosity in sandstone is cemented by carbonate precipitates, affecting dissolved CO₂ flow paths at the Little Garde Wash Fault, Utah (e.g., Fig. 1a-b). Several other examples demonstrating macroscopic characteristics of calcium carbonate (CaCO₃) precipitation in Figure 1 include an elongated concretion along the groundwater flow direction, CaCO₃ precipitation along the vertical

pathway sealed by a low-permeability layer, and calcite-cemented hanging-wall damage/mixed zone impacting permeability and flow paths. Continuum-scale reactive transport modeling has been studied for mineral precipitation and its impact on permeability (e.g., Steefel and Lasaga 1990, 1994). The numerical studies suggest that diffusion-controlled precipitate can armor fractures and limit the amount of mixing and subsequent reaction (Steefel and Lichtner 1994, 1998). Recently, mineral precipitation and its impact on flow alteration at the pore scale was evaluated under representative flow and mixing conditions in porous media (Tartakovsky et al. 2008; Zhang et al. 2010a; Yoon et al. 2012; Boyd et al. 2014). In these works, experimental and numerical pore-scale reactive transport investigations demonstrated that both thermodynamic and kinetic constraints affect precipitation rates, the distribution of mineral polymorphs, and the corresponding extent of porosity occlusion. Elemental analysis also suggested that crystal growth rates are affected by solution chemistry and location of reaction zones. In addition, other experimental results revealed the important effect of mineral formation on the estimation of diffusion coefficient (Navarre-Sitchler et al. 2009), overall reactive surface area (Navarre-Sitchler and Brantley 2007), and reactive surface area within connected pores (Landrot et al. 2012). Hence, accuracy of large-scale rate estimates depends on the type of reaction, pore geometry, reactive surface characteristics, reaction kinetics, macroscopic concentration gradient, and interaction between reaction and flow paths. As suggested in Battiato et al. (2011) and Steefel et al. (2013), Darcy-scale simulation with effective parameters may not account for nonlinear reactive transport processes associated with localized precipitation and dissolution of mineral phases.

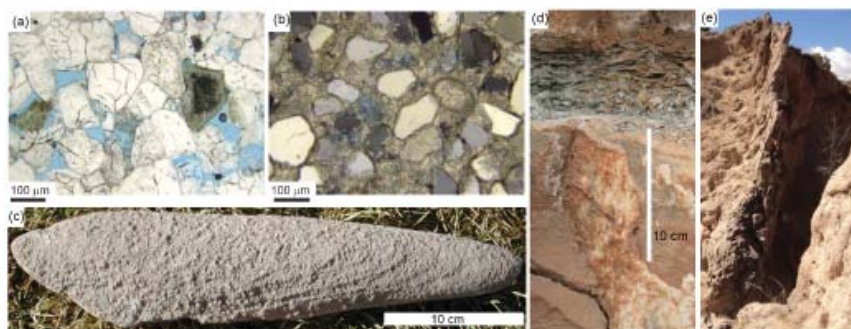


Figure 1. Examples of various mineral precipitation characteristics. Microphotographs of (a) unaltered and (b) altered sandstone in the vicinity of a natural CO₂ seepage conduit (Little Grand Wash Fault, Utah) [Used by permission of the American Chemical Society, from Altman et al. (2014) *Journal of Physical Chemistry C*, Vol. 118, Fig. 2, p. 15106]. Primary porosity in blue epoxy in (a) is altered by carbonate precipitates shown in (b). (c) Uniform elongate concretion from the Sierra Ladrones Formation (ancestral Rio Grande sediments, see Mozley and Davis (2005) for further information). (d) CaCO₃ precipitation along the vertical pathway sealed by a thin Mancos shale layer (Carmel Formation, Utah). (e) Calcite-cemented hanging-wall damage/mixed zone of the Sand Hill Fault, New Mexico (scale: >10 m).

Another notable example of porosity and permeability alteration due to reactive transport is microbial growth and the associated biogeochemical reaction products, such as biominerals. Microbial growth including extracellular polymeric substances (EPS) can significantly reduce porosity and permeability by pore plugging (Davery et al. 1998; Zhang et al. 2010b; Kirk et al. 2012; Yoon et al. 2014). Additionally, biomineralization induced by urea hydrolysis and denitrification processes (Nemati and Voordouw 2003; Dejong et al. 2006; Martin et al. 2013; Zhu et al. 2013) altered porosity and flow patterns significantly. On the other hand, organic acids (e.g. acetic acid, lactic acid, etc.) that are produced during microbial growth can dissolve rocks, resulting in increasing in porosity and permeability (Adkins et al. 1992). It is generally believed that most subsurface microorganisms are attached onto the surface of the solid phase as a

biofilm, a complex mixture of multiple active microbial species, inert biomass, and extra-cellular polymeric substances (Rittmann 1993; Rittmann and McCarty 2001; IWA Task Group 2006; Vilcáez et al. 2013). Although volume-averaging theory can be used to derive continuum-scale models, idealized geometrical assumptions about the porous media and the biofilm are necessary (Golfier et al. 2009). Instead, pore-scale numerical models capable of handling complex dynamic solid–liquid boundaries have been developed to couple flow, solute transport, and biofilm growth at the pore scale. Since biofilm dynamics at the pore scale can affect macroscopic properties such as porosity, permeability, and dispersivity (Taylor and Jaffé 1990; Vandevivere and Baveye 1992; Seifert and Engesgaard 2007; Seifert and Engesgaard 2012; El Mountassir et al. 2014; Yoon et al. 2014), the fundamentals of biogeochemical processes at the pore scale must to be understood if we are to address practical field-scale problems.

Recent advances in multiscale imaging techniques for the analysis of complex pore structures and mineralogies have revolutionized our ability to characterize geomaterials quantitatively at the pore scale (e.g., Gualda et al. 2010). By combining a suite of imaging techniques, it is now largely possible to understand how surface chemistry and pore topology impact reactive transport processes affecting the change of porosity and permeability (e.g., Landrot et al. 2012; Yoon et al. 2012). Similar recent advances in computational power and methods have led to the development of a number of pore-scale models for flow and reactive transport (see reviews in Meakin and Tartakovsky 2009; Steefel et al. 2013). To summarize, these models include lattice Boltzmann (LB) (Kang et al. 2003, 2006, 2010), smooth particle hydrodynamics (SPH) (Tartakovsky et al. 2007, 2008, 2009), direct numerical simulation (DNS) (Flukiger and Bernard 2009; Molins et al. 2012, 2014), hybrid LB-DNS (Yoon et al. 2012) and pore network models (Li et al. 2006; Kim et al. 2011). In this article we review approaches based on the lattice Boltzmann method (LBM) for pore-scale reactive transport models relevant to the impact of biogeochemical processes on the dynamic permeability evolution.

The LBM, which was developed as an extension to lattice gas models for fluid flows (Qian and Orszag 1995; Stockman et al. 1997; Chen and Doolen 1998), is well suited for studying hydrodynamics in complex geometries of porous and fractured media with a variety of reactive surface boundaries. Unlike the conventional computational fluid dynamics at the continuum scale, the LBM employs a mesoscopic equation from a kinetic theory to determine macroscopic fluid dynamics (Succi 2001). A basic introduction to the LBM for geoscientists and beginners including example (pseudo-) codes can be found in Sukop and Thorne (2007), Mohamad (2011), and open-source domains (Lattice Boltzmann methods 2015). LBM considers flow as a collective behavior of pseudo-particles residing at a mesoscopic level whose evolution is described by a discrete Boltzmann equation. Specifically, the collision term in the Boltzmann equation is approximated by the simple Bhatnagar–Gross–Krook (BGK) method (Bhatnagar et al. 1954) or single relaxation time (SRT) model. The lattice Boltzmann Equation (LBE) can be obtained from the continuum Boltzmann equation with a BGK collision term by proper discretization in time, space, and momentum (Chen and Doolen 1998). The Navier–Stokes equation can be recovered in an incompressible limit using the Chapman–Enskog multi-scale expansion technique (Wolf-Gladrow 2000). LBM can easily deal with complex boundaries using a simple bounce-back or modified bounce-back scheme (He et al. 1997) in the fluid particle distributions, and can be applied to multi-phase flow with phase transition (Chen and Doolen 1998) and particulate suspension flows (Ladd 1994; Joshi and Sun 2009). Since the LBE is an explicit time-stepping equation for the distribution function, it can be easily programmed on a computer. Based on the local nature of the kinetic reaction terms or processes, LBM is also suited for parallel computing. Recently a comparison of representative LB models for benchmark problems demonstrated a strong parallel scalability (Groen et al. 2013).

A number of studies have presented reactive transport models using LBM, focusing on crystallization processes (Miller et al. 2001; Kang et al. 2004; Lu et al. 2009), dissolution (Kelemen et al. 1995; Kang et al. 2002; Huber et al. 2008; Parmigiani et al. 2011; Chen et al. 2014b), and biofilm dynamics (Sullivan et al. 2005, 2006; Pintelon et al. 2009). In particular, Kang and co-workers have developed multicomponent reactive transport models assuming homogeneous reactions are instantaneous, and all heterogeneous reactions at the mineral–water interface are kinetically controlled (Kang et al. 2002, 2003, 2006, 2007). LBM now has expanded capabilities for (reactive) transport processes by coupling with continuum-based or DNS methods (e.g., finite-volume method (FVM), finite-element method (FEM), finite-difference method (FDM)). In this article, the lattice Boltzmann-based approaches are referred to as the LBM coupled with other techniques such as LB for flow and FVM for reactive transport. The main objective of this article is to present the current state-of-the-art in using LB-based approaches to simulate coupled flow and transport affecting pore structure change and flow feedback. In the following subsections we briefly introduce reactive transport modeling of biogeochemical processes. LBM for reactive transport models will be presented in detail. We also describe recent advances in LB applications to multiphysics systems useful for multiphase flow and electrical transport, and coupled LB–DNS approaches for reactive transport models. Representative LB-based simulations will be reviewed to demonstrate its usefulness in pore-scale reactive transport processes and future research directions will be addressed.

REACTIVE TRANSPORT MODELING OF BIOGEOCHEMICAL PROCESSES AT THE PORE SCALE

Multicomponent reactive transport models have been well outlined for a basic continuum theory for reactive transport (Lichtner 1985, 1996) and biofilm modeling in water and wastewater treatment (Rittmann and McCarty 2001; IWA Task Group 2006). Recently, pore-scale reactive transport modeling has been actively developed and applied, which were fundamentally overviewed for multiphase flow and reactive transport models (Meakin and Tartakovsky 2009) and pore-scale processes during geologic carbon storage (Steefel et al. 2013). In this section, the mathematical equations for reactive transport modeling at the pore scale will be briefly described for the rest of article and key biogeochemical processes relevant to pore structure dynamics will be introduced. The primary aspects of a reactive transport model include (1) governing equations for fluid flow, (2) transport equations for multiple species, (3) (bio)geochemical reaction models describing homogeneous reactions (reactions within a single phase) and heterogeneous reactions at the interface of different phases, and (4) the motion of the heterogeneous interface due to the reactions.

Fluid flow

The fluid flow in porous media is influenced by inertial, viscous, and body forces. In reservoirs and natural porous media systems where the compressibility of the fluid is assumed small, the incompressible Navier–Stokes equations for the fluid flow can be described by the conservation of momentum and mass:

$$\rho \left(\frac{\partial \mathbf{u}}{\partial t} + \mathbf{u} \cdot \nabla \mathbf{u} \right) = -\nabla p + \nabla \cdot \left[\mu \left(\nabla \mathbf{u} + (\nabla \mathbf{u})^T \right) \right] + \mathbf{F}, \quad (1)$$

$$\nabla \cdot \mathbf{u} = 0, \quad (2)$$

where \mathbf{u} is the fluid velocity vector, ρ is the fluid density, p is the pressure, μ is the dynamic viscosity of the fluid, and \mathbf{F} is the body-force density including all the effective external body

forces. In Equation (1) the left-hand side represents the inertial terms and the right-hand side is written in terms of the full rate-of-deformation (stress) tensor owing to, for example, concentration-dependent viscosity. This dependence couples the flow system to the reactive transport system where the time-dependent part of the acceleration term is retained because of the concentration dependence of the viscosity (e.g., Davidson et al. 2012). In this article we will treat the concentration- (or reaction-) dependent viscosity as a special case.

If the viscosity is constant or independent of the species concentrations, the flow problem is uncoupled from the species transport. At low Reynolds numbers $Re = \rho \mathbf{u} l / \mu \ll 1$ where l is a characteristic length, the inertial terms can be neglected and under the steady conditions, the Stokes equation can be used to obtain the velocity field at the pore scale:

$$\nabla p = \mu \nabla^2 \mathbf{u} + \mathbf{F}. \quad (3)$$

The quasi-static formulation for the flow implies that the geometry of the solid phase changes slowly compared to the time scale for reactive transport unless the reactions will alter the geometry of the solid phase. We will separately treat the effect of biogeochemical reactions on the change of solid (including biofilm) phase later.

Multicomponent reactive transport

In the species transport equations at the pore scale, the detailed inclusion of fluid flow at the pore scale allows us to model the diffusion by a simple Fickian form in contrast to a dispersion term at the continuum Darcy scale. For the i -th (ion) species, the reactive transport equation at the pore scale for an incompressible flow field has a general form (Lichtner 1996):

$$\frac{\partial C_i}{\partial t} + \nabla \cdot \mathbf{J}_i = R_i, \quad (4)$$

where C_i is the concentration of the i -th species, \mathbf{J}_i is the species flux, R_i is the reaction rates at which the i -th species is produced, consumed, and decayed by (bio)chemical reactions. The total flux \mathbf{J}_i consists of advection, diffusion, and electrochemical migration terms and can be described using the Nernst–Planck equation (Levich 1962):

$$\mathbf{J}_i = \mathbf{u} C_i - D_i \nabla C_i - \frac{z_i F}{RT} D_i C_i \nabla \Phi, \quad (5)$$

where D_i is the diffusion coefficient of the i -th species, z_i is the charge of the i -th species, F is the Faraday constant, R is the ideal gas constant, T is the temperature, Φ is the electrical potential. The multispecies diffusive fluxes including the electrochemical migration can be important in dilute solutions (Van Cappellen and Gaillard 1996; Li et al. 2007; Lichtner and Kang 2007; Liu et al. 2011; Molins et al. 2012; Zhang and Klapper 2014). In this article, we will briefly introduce the lattice Poisson–Boltzmann method to account for the electroosmotic flows as a special case. For the sake of simplicity, it is assumed that all ion species have the same diffusion coefficient to ensure local charge balance (Lichtner 1985) and avoid complicated charge-separation and charge-induced electrostatic interaction. The pore-scale advection–diffusion–reaction equation is

$$\frac{\partial C_i}{\partial t} + (\mathbf{u} \cdot \nabla) C_i = \nabla \cdot (D_i \nabla C_i) + \sum_{r=1}^{N_R} v_{ir} R_r \quad (6)$$

where N_R is the number of possible homogenous and heterogeneous reactions, v_{ir} is the stoichiometric coefficient, and R_r is the reaction rate.

To solve for a chemical system with many species, it is practically accepted to assume local partial equilibrium where both local equilibrium and kinetic reactions take place simultaneously. In this article, the homogeneous reactions are assumed to be in instantaneous equilibrium and all reactions at the heterogeneous interfaces are kinetically controlled. This approach is comprehensively discussed by Lichtner (1985, 1996) and the reactive transport equations in terms of the total concentrations (Ψ_j) are given by

$$\frac{\partial \Psi_j}{\partial t} + (\mathbf{u} \cdot \nabla) \Psi_j - \nabla \cdot (D_j \nabla \Psi_j) = - \sum_{k=1}^{N_m} v_{jk} R_k + R_{\text{bio}}, \quad (7)$$

$$\Psi_j = C_j + \sum_{i=1}^{N_{\text{eq}}} v_{ji} C_i, \quad (8)$$

where N_m is the number of kinetically controlled reactions, v_{jk} is the stoichiometric coefficient in the reaction k with primary species j , R_k is the reaction rate for the k -th mineral reaction at the mineral–fluid interface, R_{bio} is the reaction rate due to biologically mediated reactions (biomass growth and biological production), C_j is the concentration of primary species j , N_{eq} is the number of secondary species (subject to equilibrium reaction), and C_i is the concentration of secondary species i . The C_i is given through the mass action law as functions of the primary species concentrations:

$$C_i = \gamma_i^{-1} K_i \prod_{j=1}^{N_p} (\gamma_j C_j)^{v_{ji}}, \quad (9)$$

where γ_i is the activity coefficient and K_i is the equilibrium constant.

Mineral precipitation and dissolution

The rate laws for mineral precipitation and dissolution at the pore scale can be described by transition state theory (TST) (Lasaga 1981) where the rate law is a function of the saturation state of the solution. The reaction rate can be expressed for all minerals (Lasaga 1998) with a general form by

$$R_m = -a_m k_m \left(1 - \frac{Q_s}{K_{\text{eq}}} \right)^n, \quad (10)$$

where a_m is the specific surface area of the m -th mineral, k_m is the reaction rate constant, Q_s is the ion activity product, K_{eq} is the equilibrium constant of the reaction, and n is the order of the reaction. The limitations of the applicability of the TST rate expressions were recently reviewed by Steefel et al. (2013) to address the issues on the reversibility implied in the TST formulation, the bulk TST approaches compared to atomistic reaction processes, the lack of time-dependent mineral surface reactivity, and the limitations on transport-controlled reactions. Nonetheless, recent pore-scale modeling results (Molins et al. 2012; Yoon et al. 2012; Hiorth et al. 2013) show that the TST approaches in a form of Equation (10) can match experimental results relatively well if a fine spatial resolution (at the order of micron scale) is used together with well-characterized reaction surfaces.

As stated earlier, all mineral precipitation and dissolution will take place at the mineral–fluid interface. In addition, the rate of the change of the interface due to Equation (10) is much

slower than the scale of fluid velocities, and a quasi-steady approximation of the fluid flow can be used. Assuming no-slip boundary condition at the mineral surface, heterogeneous reactions at mineral interfaces can be represented through the internal boundary conditions (Kang et al. 2002; Li et al. 2008; Meakin and Tartakovsky 2009). The boundary condition for the total concentration is given by (Kang et al. 2006)

$$D \frac{\partial \Psi_j}{\partial \mathbf{n}} = - \sum_{m=1}^{N_m} v_{jm} k_m \left(1 - \frac{Q_s}{K_{\text{eq}}} \right)^n, \quad (11)$$

where \mathbf{n} is the direction normal to the interface pointing toward the fluid phase. Recently, Huber et al. (2014) demonstrated the phase field approach is equivalent to the internal boundary conditions in the framework of LB formulations. It is noted that when the internal boundary conditions (i.e., reaction models) are solved with the advection–diffusion equation (Eqn. 7), the configuration of the surface area and update of the surface are the key to control the overall reaction rate and the feedback between porosity change and flow field. Two key dimensionless numbers including the Péclet number ($\text{Pe} = |\mathbf{u}|l / D_m$) and the Damköhler number ($\text{Da} = k_m l / D_m$) are often used to characterize the transport and reaction processes. Since the solid phase is assumed immobile, the volume change of the mineral phase is given by

$$\frac{\partial V_m}{\partial t} = \bar{V}_m a_m R_m, \quad (12)$$

where V_m , \bar{V}_m , and a_m are the volumetric fraction, molar volume, and specific surface area of the m -th mineral, respectively. Solute diffusion in the solid phase is neglected. The volume is updated at each time step explicitly according to the equation

$$V_m(t + dt) = V_m(t) + \bar{V}_m a_m R_m \times dt, \quad (13)$$

where dt is the time interval for the mineral update.

Biofilm dynamics

A great deal of understanding biofilm dynamics has been gained from study of water and wastewater treatment processes where the bacteria are attached to a solid media forming an immobile biofilm. Modeling biofilms in engineered reactors is well described by Rittmann and McCarty (2001) and IWA Task Group (2006). Following these works, the biofilm in porous media is typically assumed to be impermeable to water flow, and therefore the total pore space can be partitioned into a fluid and biofilm phase. Dissolved substrates and solutes are allowed to diffuse within the biofilms where the diffusion coefficient within the biofilm phase (e.g., Eqn. 6 or 7) is generally taken as roughly 80% of its value in water (Rittmann and McCarty 2001). In addition, several works have allowed the biofilm to be slightly permeable to water flow to improve model predictions (Thullner and Baveye 2008; Pintelon et al. 2012; Deng et al. 2013). Assuming all the bacteria are attached to the solid as a biofilm, a local mass balance equation applies, similar to the case of mineral precipitation and dissolution

$$\frac{dM}{dt} = r_{\text{growth}} - r_{\text{decay}}, \quad (14)$$

where M represents the mass of bacteria per unit volume of fluid and r_{growth} and r_{decay} represent the bacteria growth and decay rates, respectively.

The Monod equation is widely used to link bacteria growth to consumption of dissolved substrates

$$r_{\text{growth}} = MY r_{\text{util}}, \quad (15)$$

$$r_{\text{util}} = k_{\text{max}} \frac{C}{K_c + C}, \quad (16)$$

where Y is the biomass yield coefficient (mass of bacteria produced per mass of substrate consumed), C is the dissolved substrate concentration (mass per volume fluid), k_{max} is the maximum specific utilization rate (mass of substrate per mass of bacteria-time), and K_c is the half-maximum-rate concentration. For the sake of simplicity it is assumed that there is a single limiting substrate for bacteria growth; however, several studies have used dual Monod kinetics to investigate situations where two substrates (e.g. an electron donor and acceptor) are limiting (Knutson et al. 2005; Tang et al. 2013).

The growth rate is directly coupled to substrate consumption, so formally $r_{\text{growth}} = -R_{\text{bio}}$ in Equation (7). As biomass grows, it can spread out and occupy an increasing volume of the pore space. This biofilm growth is very similar to growth of solid phase due to net precipitation, which will be discussed in the LB section. Growing bacteria requires energy for basic cell maintenance, resulting in a continuous biomass decay, termed endogenous decay (Rittmann and McCarty 2001). It is typically accepted to use a simple first-order rate law $r_{\text{decay}} = k_d M$ where k_d is a decay coefficient (1/time). In some multispecies models, a portion of the biomass that decays accumulates into a pool of inert biomass. There are other mechanisms for biofilm loss that result from discrete events over time, including cell lysis and detachment. These will be briefly discussed later. Typically, two different strategies have been used for biomass spreading, namely continuous and discrete models (Fig. 2). The first approach treats biomass as a separate continuum phase (the fluid being the other phase); the bacteria grow in response to substrate in the fluid phase and this growth leads to an expansion into the fluid domain. In discrete models, the biomass is represented as discrete quantities, either assigned to numerical grid blocks or to particles. In the discrete approach, bacteria consume substrate and grow, but the spreading process uses rules to spread the biofilm. Attachment and these spreading approaches will be described in the next section.

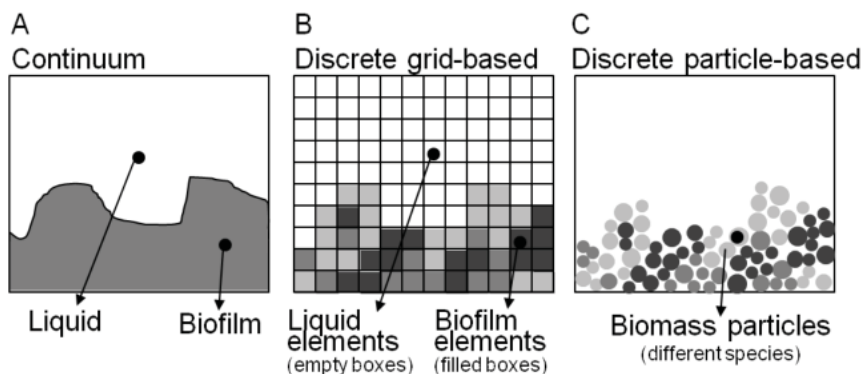


Figure 2. Biofilm growth and spreading models assume that the biofilm is either represented as a continuum (A) or as discrete quantities (B and C) [Used by permission of IWA Publishing, modified from IWA Task Group on Biofilm Modeling (2006), Fig. 3.12, p. 106].

LATTICE BOLTZMANN METHODS FOR FLOW AND REACTIVE TRANSPORT

LBM for fluid dynamics

In LBM, a fluid is treated as mesoscale particles moving in a lattice domain (space discretization) with discrete lattice velocities (momentum discretization) at discrete time steps (time discretization). The fluid variables (such as density and velocity) can be obtained through the moments (summation) of distribution functions over all discrete velocities. Typically the two-dimensional nine-velocity (D2Q9) and the three-dimensional nineteen-velocity (D3Q19) models for the 2-D and 3-D space, respectively, are employed (Fig. 3). The most popular LB fluid flow model is the Bhatnagar–Gross–Krook (BGK) or single relaxation time (SRT) model (Bhatnagar et al. 1954). However, a viscosity-dependent permeability is usually obtained when adopting SRT-LBM for simulating fluid flow in porous media (Pan et al. 2006). In order to overcome such defect, the multi-relaxation-time (MRT) model has been proposed for flow simulation (d’Humières et al. 2002; Pan et al. 2006). For a general purpose, we choose a 3-D multiple-relaxation time (MRT)-LBM in this article, because the MRT-LBM model has been shown to be superior to the SRT method (Pan et al. 2006; Hilpert 2011).

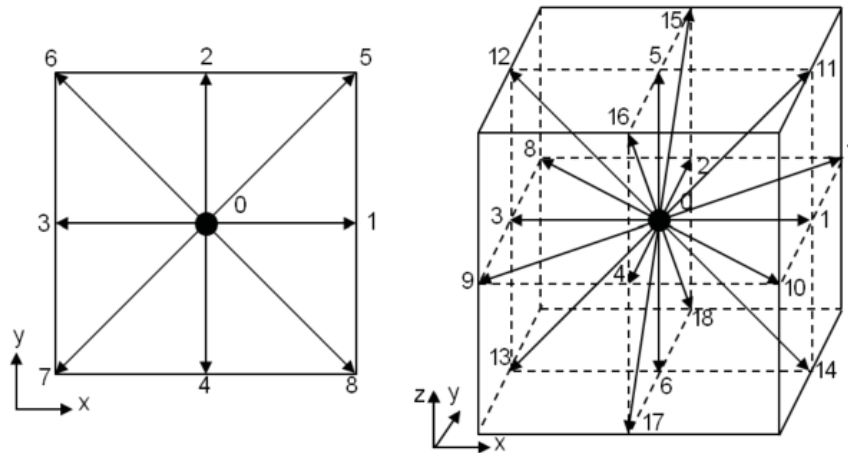


Figure 3. Schematics of the D2Q9 (left) and D3Q19 (right) models. The lattice velocities are indicated by arrows starting from the square/cube center. Note there is a zero lattice velocity $\mathbf{e}_0 = \mathbf{0}$ in both the models.

Multiple Relaxation Time LBM. The MRT-LBM model transforms the distribution functions in the velocity space of the SRT-LBM model to the moment space by adopting a transformation matrix. In the SRT-LBM model, the evolution equation for the distribution functions (i.e., LBE) can be written as

$$f_i(\mathbf{x} + \mathbf{e}_i \Delta t, t + \Delta t) - f_i(\mathbf{x}, t) = \mathbf{S}[f_i^{\text{eq}}(\mathbf{x}, t) - f_i(\mathbf{x}, t)] \quad i = 0 \sim N, \quad (17)$$

where $f_i(\mathbf{x}, t)$ is the i -th density distribution function at the lattice site \mathbf{x} and time t . \mathbf{S} is the relaxation matrix. For the D3Q19 model with $N = 18$, the discrete lattice velocity \mathbf{e}_i is given by

$$\mathbf{e}_i = \begin{cases} \mathbf{0} & i = 0 \\ (\pm 1, 0, 0), (0, \pm 1, 0), (0, \pm 1, 0) & i = 1 \sim 6 \\ (\pm 1, \pm 1, 0), (0, \pm 1, \pm 1), (\pm 1, 0, \pm 1) & i = 7 \sim 18. \end{cases} \quad (18)$$

f_i^{eq} is the i -th equilibrium distribution function and is a function of local density and velocity

$$f_i^{\text{eq}} = w_i \rho \left[1 + \frac{\mathbf{e}_i \cdot \mathbf{u}}{(c_s)^2} + \frac{(\mathbf{e}_i \cdot \mathbf{u})^2}{2(c_s)^4} - \frac{\mathbf{u} \cdot \mathbf{u}}{2(c_s)^2} \right] \quad (19)$$

with the weight coefficient w_i as $w_i = 1/3$ for $i = 0$; $w_i = 1/18$ for $i = 1, 2, \dots, 6$; $w_i = 1/36$, for $i = 7, 8, \dots, 18$. $c_s = 1/\sqrt{3}$ is the speed of sound. By multiplying both sides of Equation (17) with a transformation matrix \mathbf{Q} , an $(N + 1) \times (N + 1)$ matrix, the evolution equation in the moment space can be expressed as

$$\mathbf{m}(\mathbf{x} + c\Delta t, t + \Delta t) - \mathbf{m}(\mathbf{x}, t) = \hat{\mathbf{S}}[\mathbf{m}^{\text{eq}}(\mathbf{x}, t) - \mathbf{m}(\mathbf{x}, t)] \quad (20)$$

$$\mathbf{m} = \mathbf{Q} \cdot \mathbf{f}, \quad \mathbf{m}^{\text{eq}} = \mathbf{Q} \cdot \mathbf{f}^{\text{eq}}, \quad \hat{\mathbf{S}} = \mathbf{Q} \cdot \mathbf{S} \cdot \mathbf{Q}^{-1}, \quad (21)$$

where \mathbf{m} and \mathbf{m}^{eq} are the velocity moments and equilibrium velocity moments, respectively. \mathbf{Q}^{-1} is the inverse matrix of \mathbf{Q} , both of which are given in d'Humières et al. (2002). The transformation matrix \mathbf{Q} is constructed based on the principle that the relaxation matrix $\hat{\mathbf{S}}$, an $(N + 1) \times (N + 1)$ matrix, in moment space can be reduced to the diagonal matrix, namely

$$\hat{\mathbf{S}} = \text{diag}(s_0, s_1, \dots, s_{17}, s_{18}) \quad (22)$$

There is a large degree of freedom in choosing the relaxation parameters. According to Pan et al. (2006), one optimal set of relaxation parameters is given as:

$$s_0 = s_3 = s_5 = s_7 = 0, \quad s_1 = s_2 = s_{9-15} = \frac{1}{\tau}, \quad s_4 = s_6 = s_8 = s_{16-18} = 8 \frac{2\tau - 1}{8\tau - 1}, \quad (23)$$

where τ is related to the fluid viscosity by

$$\tau = \frac{\nu}{c_s^2 \Delta t} + 0.5, \quad (24)$$

which is called the two-relaxation-time (TRT) model (Ginzburg and d'Humières 2003).

The detailed equilibrium velocity moments \mathbf{m}^{eq} can be found in Pan et al. (2006) and density and momentum (\mathbf{j}) are determined by

$$\rho = \sum_i f_i, \quad \mathbf{j} = \sum_i f_i \mathbf{e}_i \quad (25)$$

The expression in Pan et al. (2006) includes the mean density of the fluid (ρ_0), which is employed to reduce the compressibility effects of the model. Equations (20–25) can recover the Navier–Stokes equations using Chapman–Enskog multiscale expansion under the low Mach number limitation. In contrast to the SRT model, the collision step in the MRT model is implemented in the moment space, while the streaming step is carried out in the velocity space.

Boundary conditions. As described earlier, complex geometries (boundaries) of porous media can be easily treated. A no-slip boundary condition at the solid surface can be realized through the “bounce-back” condition, which mimics the phenomenon that a particle reflects its momentum when colliding with a solid surface. It has been recognized that the combination of the SRT-LBM model with a standard bounce-back (SBB) scheme for fluid–solid boundaries may lead to viscosity-dependent permeability (Pan et al. 2006), causing errors in boundary

locations. Recently, several schemes have been developed to more accurately represent such boundaries using spatial interpolations, including the linearly interpolated bounce-back (LIBB) scheme, the quadratically interpolated bounce-back (QIBB) scheme, and the multireflection (MR) scheme (Bouzidi et al. 2001; Ginzburg and d’Humières 2003; Yu et al. 2003). These methods have been incorporated separately into SRT-LBM and MRT-LBM, and a systematic quantitative comparison of the numerical accuracy and convergence rate of these methods for complex porous medium systems has been reported by Pan et al. (2006). In their work, the MRT models significantly reduce the viscosity dependence of permeability in porous medium simulations. In the MRT models, the location where the exact flow boundary conditions are satisfied can be essentially viscosity-independent by specifying an appropriately constructed collision operator, but it is impossible to achieve this with an SRT model.

LBM for multi-component reactive transport

Advection–diffusion reaction for a single-component system. The LB models for chemically reacting fluid flows were first introduced by Kingdon and Schofield (1992) and Dawson et al. (1993). In their models, the LB equations for transport have a similar form to the flow equation, with the addition of a source/sink term representing chemical reactions. The chemical reactions used in Kingdon and Schofield (1992) represent the Selkov model. In a more general case, homogeneous chemical reactions taking place in an aqueous fluid can be written as a mass action law as in Equation (9). If the concentrations of the aqueous species are assumed to be sufficiently low so that their effect on the density and velocity of the solution is negligible, then the reactive transport of solute species can be described using another set of distribution functions, $g_{\alpha k}$, which satisfies a similar evolution equation as f_i .

$$g_{\alpha k}(\mathbf{x} + \mathbf{e}_\alpha \delta_t, t + \delta_t) = g_{\alpha k}(\mathbf{x}, t) - \frac{g_{\alpha k}(\mathbf{x}, t) - g_{\alpha k}^{\text{eq}}(C_k, \mathbf{u})}{\tau_k} + \omega_\alpha \sum_{r=1}^{N_R} v_{kr} I_r, \quad (k = 1, \dots, N), \quad (26)$$

where I_r is the reaction rate of the r -th reaction, C_k is the solute concentration of the k -th species, and τ_k is the relaxation time related to the diffusivity.

It is noted that the advection–diffusion equation obeyed by the concentration is linear in velocity \mathbf{u} . This indicates that the equilibrium distributions for scalar transport need only to be linear in \mathbf{u} ; and thus lattices with fewer vectors are sufficient for scalar transport. Thus, a reduced D2Q5 lattice model in which the discrete velocities ($i = 5, 6, 7, 8$) in the D2Q9 model (Fig. 3) are not considered, is often used for solute transport. The D2Q5 model is combined with an equilibrium distribution function that is linear in \mathbf{u} (Sullivan et al. 2005)

$$g_{\alpha k}^{\text{eq}} = C_k (J_{\alpha k} + \frac{1}{2} \mathbf{e}_\alpha \cdot \mathbf{u}) \quad (27)$$

where the concentration C_k and a constant $J_{\alpha k}$ are given by

$$C_k = \sum_{\alpha} g_{\alpha k} \quad (28)$$

$$J_{\alpha k} = \begin{cases} J_{0k}, & \alpha = 0 \\ (1 - J_{0k})/4, & \alpha = 1, 2, 3, 4 \end{cases} \quad (29)$$

The rest fraction J_0 can be selected from 0 to 1. In the literature, different forms of equilibrium distribution functions are adopted. The equilibrium distribution function given by Equation (29) is a general formula, which becomes the one used in Huber et al. (2008) if $J_0 = 1/3$ and Kang et al. (2007) if $J_0 = 0$. The accuracy and efficiency of the reduced D2Q5 model

has been confirmed in the literature (Kang et al. 2007; Huber et al. 2008; Chen et al. 2012, 2013a, 2014a). Equation (29) covers a wide range of diffusivity by adjusting J_0 , which is a prominent advantage of such an equilibrium distribution (Sullivan et al. 2005; Chen et al. 2013b). Using the Chapman–Enskog expansion technique, one can prove that Equation (26) recovers the pore-scale advection–diffusion–reaction equation for an incompressible flow field as in Equation (6). The physical diffusion coefficient using the LB parameters is given by

$$D_k = \frac{1}{2}(1 - J_{0k})(\tau_k - 0.5)\frac{\Delta x^2}{\Delta t}. \quad (30)$$

Therefore, one can solve the reactive transport problem by solving Equation (26) for each species, assuming all reaction rate constants are known.

LBM for reactive species has been used for various problems. Dawson et al. (1993) simulated pure diffusion, homogeneous chemical reactions and pattern formation due to Turing instability. Their LB simulation results agreed well with theoretical predictions and captured the basic physics as predicted by the macroscopic reaction–diffusion equations. Weimar and Boon (1996) simulated an athermal flow that advects reactant species. They considered a nonlinear reactive system described by the Brusselator model. Yan and Yuan (2001) simulated the Belousov–Zhabotinskii reaction and showed that the LBM could capture the well-known chemical clock of the diffusion–reaction system. Recently it has also been used to simulate bacterial chemotaxis (Hilpert 2005) and bacterial growth in porous media (Zhang et al. 2010b).

Advection–diffusion reaction for multi-component system. As described earlier, solving Equation (26) for each species corresponding to Equation (6) may be very computationally expensive. For multi-component systems, Kang et al. (2006) have derived the following LB equation for the total primary species concentrations, Ψ_j (Eqn. 7) with reactions written in canonical form

$$G_{\alpha j}(\mathbf{x} + \mathbf{e}_\alpha \delta_t, t + \delta_t) = G_{\alpha j}(\mathbf{x}, t) - \frac{G_{\alpha j}(\mathbf{x}, t) - G_{\alpha j}^{eq}(\Psi_j, \mathbf{u})}{\tau_{aq}}, (j = 1, \dots, N_C), \quad (31)$$

where $j = 1, \dots, N_C$ and N_C is the number of primary species, $G_{\alpha j}$ is its distribution function along the α direction, $G_{\alpha j}^{eq}$ is the corresponding equilibrium distribution function and τ_{aq} is the dimensionless relaxation time for all the aqueous species. With the homogeneous reactions in the canonical form, formulating a LB equation for total concentration Ψ_j and replacing the rates of these reactions with mass action equations, the number of unknowns and evolution equations is reduced from $N_C + N_R$ to N_C . The reduction can be significant for a system with many aqueous species. For example, the chemical system of $\text{Na}^+ - \text{Ca}^{2+} - \text{Mg}^{2+} - \text{H}^+ - \text{SO}_4^{2-} - \text{Cl}^- - \text{CO}_2$ with the reaction of calcite to form dolomite and gypsum has $(N_C + N_R)$ equal to 23, but N_C equal to only 7 (Kang et al. 2010). Here only species-independent diffusion is considered, guaranteeing conservation of charge in the aqueous phase as described earlier. Different diffusion coefficients can be obtained by varying Δx or Δt in Equation (30). More information on LBM simulation of electrochemical systems that includes species-dependent diffusion can be found in He and Li (2000) and will be briefly introduced later. Equation (31) can recover the pore-scale advection–diffusion equation without reaction terms in Equation (7).

LBM for chemical reactions at the fluid–solid interfaces. Early work on chemical reactions at solid surfaces was based on LGA. Wells et al. (1991) pioneered an LGA model that couples solute transport with chemical reactions at mineral surfaces and in pore networks. In their model, chemical reactions considered at solid surfaces included precipitation/dissolution,

sorption and catalytic reaction. Dissolution and precipitation reactions were simulated by allowing wall nodes to serve as sources or sinks for mass of a dissolved component. Whenever a particle collides with a wall, a unit of mass may be exchanged, thus increasing or decreasing the local concentration in solution depending upon the saturation state of the fluid. Later, Sullivan et al. (2005, 2006) simulated 2-D and 3-D packed bed reactors using a LBM. They accounted for the local fluid velocity by including reaction via concentration changes in the equilibrium distribution. Recently, Huber et al. (2014) treated heterogeneous reactions at the fluid–mineral interfaces which are explicitly part of the computational domain. So the internal fluid–solid boundaries are treated in a similar way as any fluid site in the computational domain, and the algorithm to solve for surface reactions is independent of the surface shape and orientation of the grains.

Typically heterogeneous reactions in the LBM are treated through boundary conditions. Kelemen et al. (1995) extended the LBM with a dissolution boundary condition such that the fluid particle colliding with the wall has a probability of detaching a solid particle. Verhaeghe et al. (2006) designed boundary conditions to impose a concentration or a flux on a solid interface for use in multicomponent LBMs. Other approaches for concentration boundary treatment focused on deriving the unknown distribution functions at the fluid–solid interface based on local conditions for different boundary condition types. To discuss the concentration boundary conditions, a schematic illustration of the fluid–solid interface is presented in Figure 4. Following Zhang et al. (2012), the boundary condition at this interface is

$$b_1 \frac{\partial C}{\partial \mathbf{n}} + b_2 C = b_3, \quad (32)$$

which is a general formula that can describe all the three types of boundary conditions: the Dirichlet boundary condition, with $b_1 = 0$ and $b_2 \neq 0$, the Neumann boundary condition, with $b_2 = 0$ and $b_1 \neq 0$, and a mixed boundary condition, with $b_1 \neq 0$ and $b_2 \neq 0$.

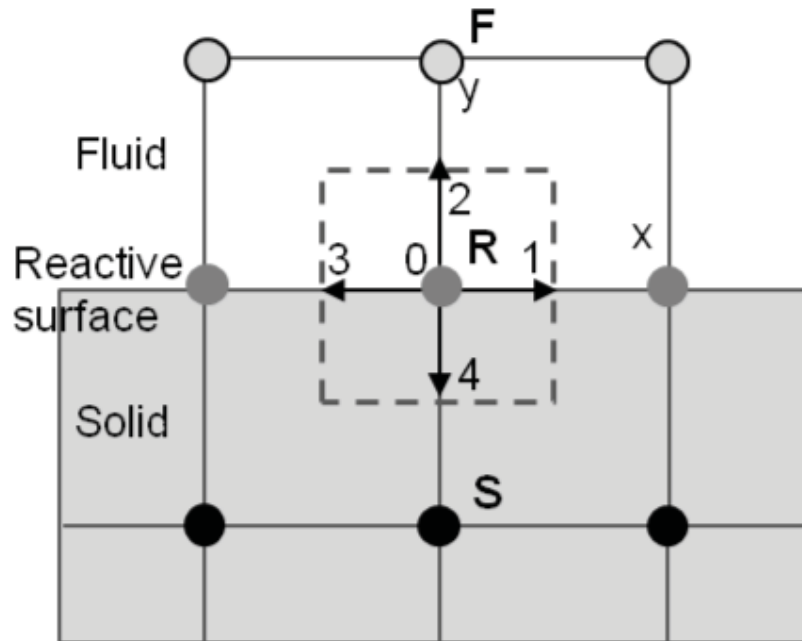


Figure 4. A schematic illustration of a fluid–solid interface node in the D2Q5 lattice model. F and S represent a fluid and solid node, respectively. R represents the reactive interface node.

Kang et al. (2007) proposed a new expression of the concentration distribution function in terms of the corresponding concentration and its gradient

$$\sum g_i \mathbf{e}_i = \mathbf{C}\mathbf{u} - D\nabla C. \quad (33)$$

After each streaming step in Figure 4, g_2 is unknown and g_4 is known; and g_1 and g_3 do not affect the fluid domain and hence are not needed to calculate their values. In this case, the reactive wall is static. They pointed out that since g_2 enters the domain and g_4 leaves the domain, the following equation based on Equation (33) is obtained at the reactive node R

$$g_2 - g_4 = -\frac{D}{c} \frac{\partial C}{\partial y} = \frac{k_m}{c} \left(1 - \frac{Q_m}{K_m} \right), \quad (34)$$

where $c = dx/dt$ and C can be the total concentration for the multi-component system. The fact that the non-equilibrium portion of the distribution functions in opposite directions takes the opposite sign for a static wall derives another equation

$$g_2 + g_4 = (g_2^{\text{eq}} + g_2^{\text{neq}}) + (g_4^{\text{eq}} + g_4^{\text{neq}}) = g_2^{\text{eq}} + g_4^{\text{eq}}. \quad (35)$$

Finally, the unknown distribution g_2 can be obtained by combining Equations (34–35).

Instead of using Equation (33), Zhang et al. (2012) proposed to directly solve Equation (32) to obtain the concentration at the boundary using the following difference scheme

$$b_1 \frac{C_R - C_F}{|\Delta x|} + b_2 C = b_3, \quad (36)$$

where C_R and C_F are the concentrations at interface node R and adjacent fluid node F, respectively, and Δx is the distance between nodes F and R. In Equation (36) C_R is the only unknown and thus can be directly solved. The unknown g_2 can be solved with Equation (35). Following Zhang et al. (2012), Chen et al. (2013b) improved the accuracy of boundary treatment by adjusting the bounce-back particle distribution functions according to the velocity and concentration values at the midpoint of a boundary lattice link.

In a recent study, Chen et al. (2013b) proposed to use Equation (33) to solve the unknown distribution function after C_R is obtained from Equation (36). For the boundary node shown in Figure 4, the new boundary condition can be written as

$$\begin{cases} b_1 \frac{C_R - C_F}{c} + b_2 C = b_3 & (a) \\ g_2 - g_4 = C_R v - \frac{D}{c} \frac{\partial C}{\partial y} & (b) \end{cases}. \quad (37)$$

Equation (37a) is used to solve C_R , followed by using Equation (37b) to solve g_2 . This boundary condition treatment can handle moving boundary conditions. The boundary condition described by Equation (37) can be uniformly used to treat both a reactive fluid–solid boundary and a zero-flux fluid–fluid boundary. For the static fluid–solid boundary, a precipitation or dissolution reaction leads to the following reduced form of Equation (37)

$$\begin{cases} D \frac{C_R - C_F}{c} = -k_m \left(1 - \frac{C_R}{K_m} \right) & (a) \\ g_2 - g_4 = -\frac{D}{c} \frac{\partial C}{\partial y} & (b). \end{cases} \quad (38)$$

For the moving fluid–fluid boundary, there is no reaction, and the concentration gradient of solute is zero. Thus Equation (37) reduces to

$$\begin{cases} D \frac{C_R - C_F}{c} = 0 & (a) \\ g_2 - g_4 = C_R v & (b). \end{cases} \quad (39)$$

Update of solid–pore geometry

To model accurately reactive transport involving significant mass transfer between solids and fluids due to dissolution and/or precipitation, it is necessary to account for the time evolution of the solid phase (pore geometry). For tracking the fluid–solid interfaces, the phase field (PF) method (Chen 2002) and the cellular automaton (CA) methods (Sun et al. 2009) are widely used. Other methods such as Volume of Fluid (VOF) and Level Set (LS) commonly used for multi-fluid phase flow, can be also adopted for this purpose (Li et al. 2008). Verberg and Ladd (2000, 2002) designed an algorithm for simulating chemical erosion in rough fractures using an optimized LB scheme. A continuous bounce-back scheme allows for the boundary to be located anywhere between two grid nodes. The new solid structure is determined based on the local flux of tracer particles across the solid surface, assuming an instantaneous reaction, so dissolution is diffusion-controlled. In Verhaeghe et al. (2006), the amount of species injected in the system was calculated from the difference between populations leaving and entering the system. Li et al. (2008) studied a similar problem using LS to track the fluid–solid interfaces. In addition, Luo et al. (2012) implemented a model using a diffuse interface method to track the fluid–solid interface. Most recently, Huber et al. (2014) combined LBM and PF method for dissolution–precipitation processes involving single or multiple species.

To track the moving fluid–solid interfaces caused by dissolution and precipitation, Kang et al. (2003, 2006) developed the volume of pixel (VOP) method, a type of CA method. Each fluid–solid interface node represents a control volume (a control area in the 2-D case) with a size of $1 \times 1 \times 1$ (in lattice units) and is located at the center of this volume. As in Figure 4, the node R is the center of the control volume surrounded by dashed lines. The control volume is assigned with a certain amount of mineral mass (volume) that changes with time due to chemical reaction (Eqn. 12); then the volume is updated using Equation (13). In these studies, both a time interval and specific surface area (a_m) equal unity in lattice units. When V_m reaches certain threshold values, the pore geometry needs to be updated. Here we will briefly describe the volume of pixel method developed by Kang and coworkers.

Single mineral VOP method. In this method, the grid size is assumed to be small enough to represent each node by one mineral at one time and the effect of both dissolution and precipitation is recorded at that node through Equation (13). For dissolution, the solid node associated with V_m can be simply removed (i.e., changed to a pore node) when V_m reaches zero (Kang et al. 2002, 2014; Chen et al. 2014a). For precipitation, when V_m reaches a certain threshold value, a nearby neighboring fluid node (child node) can be chosen to become a solid node. There may be multiple such nodes, and different ways of choosing the child node may lead to different crystal growth patterns. Therefore, the single-mineral VOP model has an extra degree of freedom which allows for incorporating different crystal growth mechanisms such as a random-growth method for single species (Kang et al. 2003, 2004) and multi-component systems (Kang et al. 2006). In this random-growth method, the growth has no preference in any particular direction and the method has been shown to be lattice-effect free. Figure 5 shows crystal growth patterns from a supersaturated solution of a single species using the random-growth method. It is clear that crystal shape in this case (d) is fairly round. The VOP has many advantages: a clear physical concept, simple and stable arithmetic, easy implementation of various surface reactions, and flexible coupling with different nucleation and crystal growth

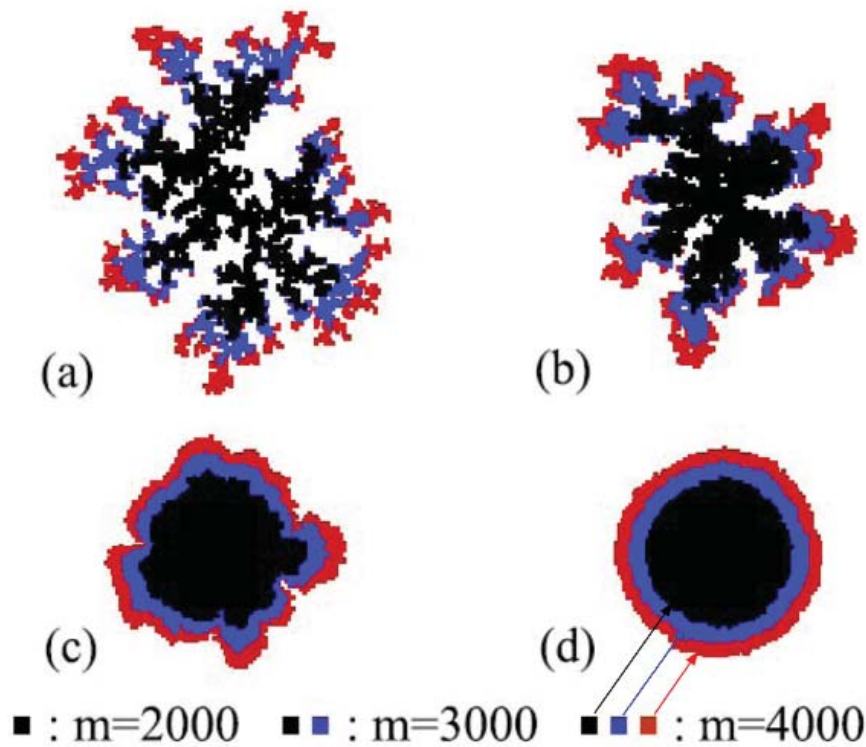


Figure 5. Crystal structures developed at different Da numbers and at solute saturation (1.2): (a) Da = 600; (b) Da = 150; (c) Da = 48; (d) Da = 2. m represents the number of solid particles (crystal mass). [Used by permission of John Wiley and Sons, from Kang Q, Zhang D, Lichtner PC, Tsimpanogiannis IN (2004) Lattice Boltzmann model for crystal growth from supersaturated solution. *Geophysical Research Letters*, Vol. 31, Fig. 2, p. L21604-3]

mechanisms. The method has been used successfully to predict many moving solid–fluid interface phenomena, such as crystal growth (Kang et al. 2004), rock dissolution due to acid injection (Kang et al. 2002, 2003), Liesegang bands or rings (Chen et al. 2012), and dissolution and precipitation involved in CO₂ sequestration (Yoon et al. 2012).

Growth in preferred directions can be achieved by exploiting the extra degree of freedom in the VOP model and incorporating corresponding physics in the growth rules. For examples, polygonal and dendritic crystals with symmetry have been produced by aligning the direction of growth to that of the maximum concentration gradient and different morphologies have also been obtained by varying the probability of adding a solid node in that direction (Lu et al. 2009). Another growth mechanism is epitaxial growth in which the precipitates quickly spread and cover the surface of the primary mineral, thus only a small amount of precipitates can completely stop the dissolution (Prieto et al. 2003).

Multiple mineral VOP method. In reality, changes of solid morphology can involve scales much smaller than the lattice or pore size used in the simulations. Therefore, it is reasonable to assume that each node can be represented by multiple minerals with the initial total volume fraction equal to unity. In this case, the volume fraction of each mineral is still updated by Equation (13) and dissolution recorded in the solid node. Mass accumulation due to precipitation, however, is recorded at the neighboring pore nodes. As seen in Figure 4, when

$$\sum V_m(R) = 0, \quad (40)$$

the node R is changed to a fluid node. Alternately, when

$$\sum V_m(F) = V^0, \quad (41)$$

the node F becomes a solid node composed of multiple minerals. In contrast to previous methods (Kang et al. 2003, 2004, 2006) for updating pore geometry, the multiple-mineral VOP method can account for coexistence of multiple minerals at the same node and the growth of minerals is deterministic rather than random. Figure 6 shows crystal structures at $Da = 600$ with the single-mineral VOP (random-growth) method (left) and multiple-mineral VOP approach (right) to update the solid phase (Kang and Lichtner 2013). At this high Da number, the process is diffusion-controlled. As a result, the crystal structure is not compact. However, while the crystal on the left is an open cluster-type structure, consistent with that of the multi-particle, diffusion-limited aggregation in the simulation of solidification structures of alloy melt, the crystal structure on the right is highly symmetric and regular. The multiple-mineral VOP approach was also used in the pore-scale study of reactive transport involved in CO_2 sequestration (Kang et al. 2010). Clearly, when combined with appropriate methods for the underlying physical properties and processes to update the solid phase, the LBM can simulate a variety of reactive flow problems.

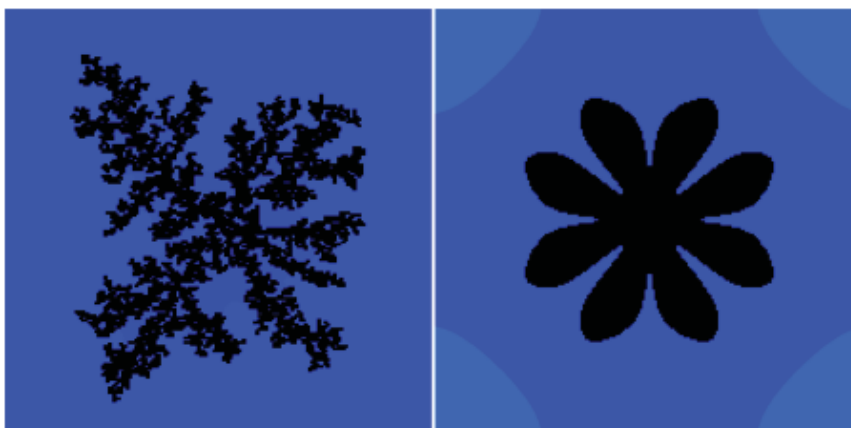


Figure 6. Crystal structures and solute concentration obtained using single-mineral VOP approach (random growth) (left) and multiple-mineral VOP approach (right). [Used by permission of Hindawi, from Kang QJ, Lichtner PC (2013) A lattice Boltzmann method for coupled fluid flow, solute transport, and chemical reaction. In: *Progress in Computational Physics*. Ehrhardt M (ed) Bentham Science Publishers, Vol. 3, Fig. 8, p. 196]

LBM for biofilm dynamics

The system of equations described in Equations (3), (6) and (14–16) includes three dynamic processes, which occur at very different time scales: biofilm development on the order of hours or days; transport and reaction of chemical species on the order of minutes; and fluid flow on the order of seconds (Picioreanu et al. 2000; Pintelon et al. 2009). Therefore, when the flow or substrate concentration suddenly changes, the biofilm can be assumed unchanged (i.e., in a “frozen” state). Based on this assumption, the three processes are commonly decoupled and solved sequentially. As described earlier, the biofilm consists of multiple active microbial species, inert biomass, and EPSs. Biofilm spreading is typically computed using a continuum or discrete model as shown in Figure 2. Since a majority of pore-scale biofilm models in literature adopt a discrete representation of the biomass, this approach will be explained in

more detail below. For continuous model of biofilm spreading, the reader may refer to key literature for various variants (Alpkvist and Klapper 2007; Wang and Zhang 2010; Lindley et al. 2012; Zhang and Klapper 2014). The LBM earlier described for hydrodynamics and reactive transport can be applied for biogeochemical reactive transport. In fact, the LBM for advection-diffusion-reaction (Eqns. 27–30) developed by Sullivan et al. (2005) for packed bed reactors was directly applied for biofilm dynamics (von der Schulenburg et al. 2009). In Sullivan et al. (2005), the diffusion coefficient within intra-particle space was adjusted by changing the relaxation time (τ_k) in Equation (30), which can be adapted for diffusivity within biofilm. Knutson et al. (2005) simulated biofilm growth in porous media to account for biofilm morphology observed in microfluidic experiments using the LB-FVM with a CA algorithm for biofilm dynamics. von der Schulenburg et al. (2009) presented the first numerical 3-D pore-scale model of biofilm growth in porous media, based on an LB simulation platform complemented with an individual-based biofilm model (IBM), where the biofilm is represented as a collection of non-overlapping hard spheres. Following this work, Pintelon et al. (2009) added a biomass detachment technique using a fast-marching level-set method that modeled the propagation of the biofilm liquid interface with a speed proportional to the adjacent velocity shear field.

Attachment. The first stage in biofilm development is its attachment to the solid surface. This is a complex process that involves deposition of suspended bacteria onto the surface followed by physiologic changes (Breyers 1988). The deposition process has been quantified using colloid filtration theory (e.g., Harvey and Garabedian 1991; see other citations in Rittmann 1993), but most of these studies address migration of bacteria in porous media. For pore-scale biofilm dynamics, some initial spatial distribution of attached biomass is typically assumed. For example, in the approach of Knutson et al. (2005) and Tang et al. (2013), the initial mass of microbes was randomly distributed among grid cells along the liquid-solid interface, a distribution which simplified the inoculation of biomass in the microfluidic pore network. A similar approach to inoculation is used by von der Schulenburg et al. (2009), whereas Bottero et al. (2013) modeled a fixed rate of attachment by converting grid cells from fluid to biomass at the liquid–solid interface at each time step; they used a random spatial pattern, but screened out solid boundaries on particles in stagnant zones.

Discrete model for biofilm growth and spreading. Following the pioneering work by Picioreanu et al. (1998), a popular approach to a discrete representation of the biomass is to assign biomass to fixed grid cells (normally squares in 2-D and cubes in 3-D). A mass balance equation applies to each biomass cell (Eqn. 14). The biomass in each cell grows due to substrate utilization, and when the total biomass in the cell exceeds a critical value, the excess biomass is spread (transported) to adjacent grid cells according to some rules such as CA as described for mineral precipitation. Many different CA rules for biomass spreading have been used in the literature; the three most common are briefly discussed here (Tang et al. 2013). In the first rule (e.g., Kreft et al. 2001), when the biomass concentration in a grid is higher than the critical value, the biomass in the source grid divides in half, similar to bacterial reproduction. One half stays in the grid, the other half displaces a randomly chosen nearest-neighbor, which in turn displaces another randomly chosen neighbor, and so on until a free liquid grid (i.e., a destination grid on the biofilm surface) is available. In the second rule (e.g., Noguera et al. 1999), the excess biomass (i.e., biomass that is greater than the maximum) is distributed directly to one of the nearest free liquid grids (i.e., destination grid) non-adjacent to the source grid cell. In the third rule (e.g., Tang and Valocchi 2013), excess biomass spreads by pushing a line of grid cells that are on the shortest path from the source grid cell to the destination grid cell, causing changes to the fractions of different biomass species in the grid cells on the path. The three different rules yield similar simulated results for a single species biofilm, but different results for multi-species biofilm (Tang and Valocchi 2013). These rules can be modified in many ways; for example, instead of distributing excess biomass to a randomly

chosen nearest neighbor, the destination grid having the highest substrate concentration can be selected. Knutson et al. (2005) and Tang and Valocchi (2013) exclude destination cells where fluid velocity or fluid shear stress is above a certain threshold, and found that this exclusion was needed to qualitatively match biofilm spreading observed in microfluidic experiments (Nambi et al. 2003; Zhang et al. 2010b).

Even with simple CA rules (e.g., Picioreanu et al. 1998), the interplay between mass transfer and biofilm growth can lead to a diverse biofilm patterns as shown in Figure 7. Initially, 20% of the surface has a randomly spaced inoculum; a limiting substrate diffuses from the upper boundary to the lower surface resulting in biofilm growth. The irregular “mushroom shaped” colonies form when the rate of diffusion is small relative to the rate of degradation at 50 days (Fig. 7). In the other discrete model (i.e., IBM), however, spherical particles grow by consuming substrate, resulting in an increased radius. When the particle mass exceeds a threshold, it divides into mother–daughter particles that spread out; a “shoving” algorithm is used to eliminate overlapping radii of particles (see Kreft et al. 2001 and Picioreanu et al. 2004 for details). Since the IBM is not constrained to grid coordinates, biofilm morphologies tend to be more rounded than those resulting from the CA approach. The latter also leads to biofilms that are artificially constrained to the underlying grid. The IBM is flexible because it can include different bacteria species along with inert biomass and other components (Picioreanu et al. 2004).

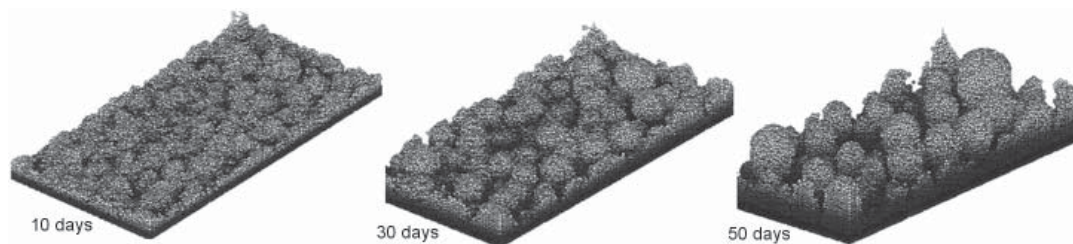


Figure 7. Developing biofilm using the CA modeling approach on a flat surface due to diffusion of a single limiting substrate from the top boundary. The system is transport limited [Used by permission of John Wiley and Sons, from Picioreanu C, van Loosdrecht MCM, Heijnen JJ (1998) Mathematical modeling of biofilm structure with a hybrid differential-discrete cellular automaton approach. *Biotechnology and Bioengineering*, Vol. 58, Fig. 6, p. 111].

Biofilm loss processes. In addition to the endogenous decay process described earlier, there are several other mechanisms for loss of mass from biofilms, including lysis, protozoan grazing, and detachment. Detachment can include several mechanisms, including erosion of small pieces from the outer surface of the biofilm and sloughing of larger sections (IWA Task Group 2006). A recent trend is to use a relatively rigorous bio-mechanical model of biofilms to study detachment and related processes (Dupin et al. 2001; Klapper and Dockery 2010; Lindley et al. 2012). Several studies adopting a discrete biofilm model use mechanical principles to simulate detachment in porous media systems. Picioreanu and co-workers treat the biofilm as an elastic solid and use classical mechanical equilibrium and compatibility conditions to determine “failure,” i.e., detachment (e.g., Picioreanu et al. 2001). This approach requires input of basic biofilm mechanical properties such as the tensile strength and elastic modulus, and is relatively straightforward to implement for 2-D CA biofilm models. von der Schulenburg et al. (2009) neglected to include detachment due to relatively lower shear rates, but Pintelon et al. (2009) used the IBM for biofilm spreading and used a fast-marching level-set (FMLS) method to simulate biomass detachment. Bottero et al. (2013) used a similar detachment model based on level sets, but allowed the cohesive strength of biofilm to decrease as biomass decays. It is one of the few studies that explicitly considers the cell lysis

mechanism; biofilm lysis occurs when the fraction of inert biomass in a grid cell exceeds a certain value. In all models, including Bottero et al. (2013), all detached biomass is assumed to be instantly removed from the system, an assumption which may not be accurate in porous media. Biofilm detachment can also be considered in pore-network models (e.g., Stewart and Kim 2004; Thullner and Baveye 2008), but these models are not covered in this article.

LB-BASED ALGORITHMS FOR OTHER APPLICATIONS

Multiphase reactive transport

There has been little work on numerical simulation of chemical processes coupled with multiphase flow at the pore scale (Meakin and Tartakovsky 2009; Parmigiani et al. 2011; Chen et al. 2013b). Although models for both single-phase multi-component reactive transport and multiphase flow have been developed, integrating the two is challenging because new physical processes absent in their respective individual system will arise due to the coupling between them. For example, the displacement patterns that range from planar fronts to capillary and viscous fingers will determine the fluid–fluid interfacial area. This interfacial area will affect chemical reactions at the interface and will change the chemical heterogeneity of the system. This chemical heterogeneity, together with the physical heterogeneity of the porous media, in turn, will influence the intrinsically complex contact line/contact angle dynamics, and hence influence the displacement patterns.

Recently, several works attempted to investigate chemical processes coupled with multiphase flow using the LBM. Parmigiani et al. (2011) studied a non-wetting fluid flowing into a wetting fluid coupled with dynamic evolution of the solid geometries due to chemical reactions. Although it was suggested that their model can be used for reactive transport with dissolution or precipitation, the demonstration was limited to only melting of the solid phase. Chen et al. (2013b) combined the LBM and the VOP to simulate multiphase reactive transport with phase transition and dissolution–precipitation processes. This pore-scale model can capture coupled non-linear multiple physicochemical processes including multiphase flow with phase separation, mass transport, chemical reaction, dissolution-precipitation, and dynamic evolution of the pore geometries. The model was used to study the thermal migration of a brine inclusion in a salt crystal. However, the pore-scale model was limited to the liquid–gas two-phase flow within a single-component water-vapor system, and the transport of only a single solute was considered. To overcome these problems, Chen et al. (2014b) developed a two-phase multi-mixture model based on the pseudo-potential LB model (Shan and Chen 1993), the mass transport LB model and the VOP model for multi-component multiphase reactive transport with dissolution–precipitation processes. After the two-phase system is constructed using a unified liquid component and a unified gas component, the mass transport of each component in the corresponding phase is solved using the mass transport LB model. The dynamic evolutions of the liquid–solid interfaces due to dissolution–precipitation reactions are captured using the VOP method.

Electrokinetic transport

Electrokinetic flow, which involves multiple processes including fluid flow, electrostatic interaction, species diffusion, and sometimes energy transfer, is pervasive both in nature and in engineered systems (Li 2004; LinkMasliyah 2006). Although numerous theories and models for large-scale electrokinetic flows have been developed for almost a century (Bancroft 1926; Li 2004), only in recent decades has the electrokinetic transport been applied at micro- and nano-scales. The Poisson–Boltzmann (PB) model, composed of a Navier–Stokes equation for fluid flow and a PB equation for electric potential distribution, has been widely used for analysis and prediction of electrokinetic flows in microchannels (Li 2004; Karniadakis et al. 2005;

Wang and Kang 2009; Wang et al. 2010a,b). The Boltzmann distribution assumption of ions in electric double layer (EDL) leads to the decoupling between the fluid flow and the ion distribution, simplifying the predictions. The lattice spacing can be based on the Debye length representing an electrical double layer thickness ($\sim 1\text{--}20$ nm for typical aqueous solutions), which was sufficient to represent the main electrolyte flow within the microchannel (e.g., Wang et al. 2008). Many algorithms and analyses based on the PB model have been proposed for understanding electrokinetic fluid mechanics and optimizing electrokinetic microdevices (Holst et al. 2000; Li 2001; Guo et al. 2005; Wang et al. 2006; Chen et al. 2007; Shi et al. 2008). However, the Boltzmann distribution is an equilibrium model with questionable applicability when ions have macroscopic motion (advection or diffusion), surface is heterogeneously charged, or the bulk solution boundary condition is not satisfied in the place sufficiently far away from the charged surface. In contrast, the dynamic model uses the Nernst–Planck equation (Eqn. 5) for ion transport instead of the hypothesized Boltzmann distribution (Levich 1962). In the dynamic model, each transport process is governed by the corresponding fundamental dynamic equation. The dynamic model has been used to validate the PB model by a few researchers (Qu and Li 2000; Yang et al. 2001; Fu et al. 2003; Kang and Suh 2006; Baldessari 2008), yet it was reported that the PB model failed in the case of overlapped double layers (Qu and Li 2000; Kang and Suh 2006).

Because the transport processes influence each other, the governing equations in the dynamic model are coupled together, posing a great challenge to the numerical solution. Wang and Kang (2010) developed a numerical framework to solve the dynamic model to study the applicability of the PB model for electrokinetic flows in microchannels using coupled LBMs. The governing equation for each transport process is solved by an LBM and the entire process is simulated iteratively. Later, Yang et al. (2014b) developed an MRT-LBM for the Nernst–Planck (NP) equation to solve the double-diffusive-convection equation having the cross diffusion effects in a channel of a $0.8\ \mu\text{m}$ width, and demonstrated that the MRT-LBM is more accurate than an SRT-LBM for the NP equation.

Coupled LBM-DNS for multicomponent reactive transport processes

Due to accurate, fine resolution representation of pore structures and flow field, pore-scale reactive transport models including LBM are often computationally expensive. The computational expense of these pore-scale models can be highlighted when the reaction occurs locally, compared to the size of model domain of interest. To overcome the computational expense of pore-scale models, a variety of hybrid methods have been developed by coupling different scale models (e.g., Weinan et al. 2007). Here we briefly introduce the recent development of coupled methods involving LBM.

LBM now has expanded capabilities for pore- and continuum-scale coupling with continuum-based methods (e.g., FVM, FDM, FEM). In the multiscale formulation, the key to improved numerical stability, accuracy, and computational efficiency is a coupling strategy to transfer information between two neighboring regimes of different methods. Luan et al. (2010) developed an analytical expression (i.e., reconstruction operator (RO)) to transfer the velocity information at the continuum scale obtained using FVM to the single-particle distribution function for LBM within the overlapping region. Furthermore, Luan et al. (2011) coupled a local grid refinement of LB (multi-block LBM) with FV for multiscale simulations and successfully demonstrated the accuracy and efficiency of the multi-block LBM for fluid flows around complex solid geometries. A coupled LB–FV method also has been adopted for different physical processes. For example, Zarghami et al. (2012) developed a cell-centered FV method for discretizing the SRT to improve the stability of the flow fields over a range of Reynolds numbers (Re). More recently, coupled LB–FV methods have been developed for reactive transport processes for multiphysics problems. Chen et al (2013a) used a multiscale modeling framework with a coarse (FVM region)-fine (LBM region) grid system to simulate

electro-chemical transport reaction in a membrane fuel cell system. They adopted RO methods (Luan et al. 2010, 2011) to transfer density, velocities, and concentration at the continuum scale (FVM) to distribution functions for density and concentration (e.g., Eqn. 17, 26) at the pore scale in the LBM and achieved a maximum grid size ratio of 10:1 between FVM and LBM regions. Following this work, a generalized RO methodology was proposed for fluid flow, heat transfer, and reactive transport processes (Chen et al. 2013b). A unified coupling scheme for coupled LB–FVM was recently developed for unsteady fluid flow and heat transfer by deriving a generalized form of RO (Tong and He 2015) where the coupling flexibility was generalized for multi-physics problems.

Hybrid approaches coupling LB for flow and FD or FV for reactive transport have also been developed for mineral precipitation and dissolution in porous media (Yu and Ladd 2010; Yoon et al. 2012). Yu and Ladd (2010) demonstrated the movement of the solid–fluid interface due to dissolution by constructing a piecewise continuous surface which can remap the surface to the regular grid system. Yoon et al. (2012) also showed that the concentration field can be solved as a steady solution and FVM can be computationally efficient for the concentration field. This hybrid approach validated the update algorithm of the solid phase against experimental data obtained in a micromodel and it demonstrated that coupling LB–FVM for reactive transport has the potential of using advanced reactive transport codes such as PFLOTRAN (Lichtner et al. 2014) with a proper interface module. Recently Patel et al. (2014) coupled the LBM for solute transport with the generic geochemical code, PHREEQC (Parkhurst and Appelo 2013). The heterogeneous reactions at the mineral–fluid interface are treated as pseudo-homogeneous reactions by incorporating an additional source (i.e., collision) term computed from the PHREEQC to the fluid node adjacent to a mineral node. This approach was validated with a set of benchmarks including the impact of pH, surface area, and arrangement of mineral grains on dissolution rate and pore structure evolution. In addition, Boek et al. (2014) recently developed a new hybrid LB and particle tracking method to study flow and reactive transport in porous media. The hybrid method used a graphical process unit (GPU) algorithm for large scale LB calculations to enhance computational efficiency. Particle advection was then solved with LB flow fields using a second-order predictor-corrector scheme, and particle diffusion with a random walk followed by heterogeneous reaction was solved.

THREE-DIMENSIONAL CHARACTERIZATION OF PORE TOPOLOGY

Over the past two decades multiscale imaging methods for geomaterials such as X-ray computed microtomography (micro-CT), laser scanning confocal microscopy (LSCM), focused ion beam-scanning electron microscopy (FIB-SEM), and energy dispersive X-ray spectroscopy (EDS) have been tremendously improved. Major advances in 3-D imaging techniques can be traced back to early 1990s when methods for characterizing geomaterials at the microscopic scale using confocal microscopy and micro-CT was established (Spanne et al. 1994; Fredrich et al. 1995; Coker et al. 1996; Coles et al. 1998). The most predominant 3-D imaging method used for geomaterials is a non-destructive micro-CT technique. Micro-CT has been used to measure the geometric properties of pore topology and multiple fluid phases at an order of microns. Theoretical and detailed technical aspects of micro-CT have been extensively reviewed by Wildenschild and Sheppard (2013) who also highlighted issues associated with the imaging process. Recently, 3-D micro-CT images of a real soil at 25 μm resolution were used to identify a mixed medium containing both pore and porous regions where small pores below the image resolution were treated as porous regions (Yang et al. 2014a). The mixed medium was then used to validate a unified multi-scale model for pore-scale flow simulations in a mixed medium by applying the Stokes–Brinkman equations for variably saturated soils.

LBM has been extensively applied for a variety of complex fluid flow problems, including single and multi-phase flow and reactive transport in complex geometries obtained from micro-CT imaging (Ladd 1994; Martys and Chen 1996; Keehm 2004; Fredrich et al. 2006; Boek et al. 2014; Jiang and Tsuji 2014; Gao et al. 2015). A major advantage of LBM is the relative ease of accounting for very complex pore-geometries from segmented image data due to its discrete dynamics (Chen and Doolen 1998). This method enables pore-scale simulations of fluid flow and transport phenomena to enhance fundamental insights in porous media. Chen et al. (2007) and Zhang (2011) provide interesting reviews and fundamentals for single and multi-phase flows, respectively. For example, 3-D rendering of the pore phase in natural Castlegate sandstone at 1.67 μm resolution from micro-CT images is shown in Figure 8a (Fredrich et al. 2006). Permeability predictions from LB simulations for 1 to 3 mm^3 image volumes show a good agreement, over 4 orders of magnitude in scale, with values measured experimentally in the core samples (25.4 mm in diameter and 50.8 mm in height). This finding revealed the representative volume and length scales that are necessary to characterize geometrically complex porous media and predict fluid transport properties at the macroscale. More recently, LB-based approaches were used to investigate the porosity dynamics due to precipitation and dissolution in 3-D pore structures from micro-CT images (Jiang and Tsuji 2014; Gao et al. 2015). These recent studies using micro-CT images can be combined with other imaging techniques (e.g., backscattered electron mapping coupled with X-ray based methods) for mineralogical distribution (Peters 2009; Landrot et al. 2012) to investigate coupled fluid flow and geochemistry, as well as the emergence of coupled behaviors due to biogeochemical reactions. Furthermore, 3-D digital representations of rock from micro-CT images and physics modeling based on these pore structures provide the opportunity to further advance our quantitative estimates of permeability, elastic moduli, and electrical conductivity of several representative 3-D rock samples (Arns et al. 2002, 2009; Andr a et al. 2013a,b).

Recently, Yoon and Dewers (2013) rigorously quantified the existence of a statistical representative elementary volume (SREV) using FIB-SEM imaging of nano-porous chalk using LB simulations with 3-D reconstructed chalk data as shown in Figure 8b. They highlighted the quantitative analysis of nano-pore structural features impacting pore-scale flow and transport properties and confirm that the size of the SREV for a sample of Gulf Coast chalk can be established at $\sim 10 \mu\text{m}$ based on anisotropic permeability, tortuosity, and specific surface area. With such clear scale separation, upscaling averaging techniques, such as homogenization, permits the application of continuum physics principles to coupled thermo-hydro-mechanical-chemical (THMC) modeling. However, porous materials with a high degree

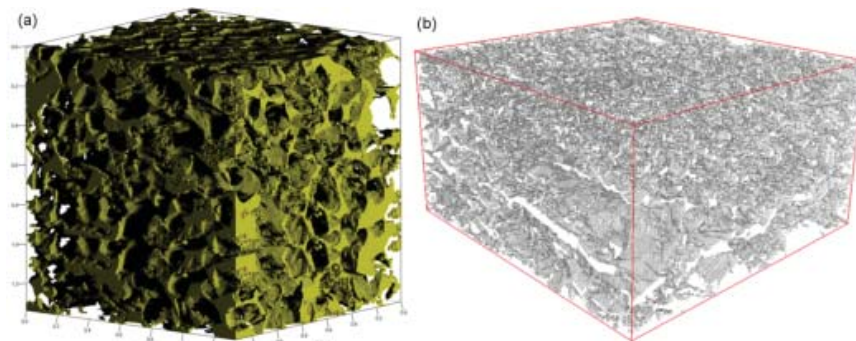


Figure 8. (a) 3-D rendering of the pore phase in natural Castlegate sandstone at image resolution of 1.67 μm [Used by permission of John Wiley and Sons, from Fredrich JT, DiGiovanni AA, Noble DR (2006) Predicting macroscopic transport properties using microscopic image data. *Journal of Geophysical Research*, Vol. 111, Fig. 7, p. B03201-10] and (b) 3-D reconstructed pore (white) topology over a sample volume of $\sim 14 \times 14 \times 10 \mu\text{m}^3$.

of physical and chemical heterogeneity exist with no clear scale separation (e.g. Bilger et al. 2005). The problem of scale relating to the traditional FIB-SEM with gallium (Ga) ion milling (e.g., sample volumes in the order of $\sim 10 \times 10 \times 10 \mu\text{m}^3$) is now being confronted, which makes the FIB-SEM analysis more qualitative than quantitative. Newly emerging techniques such as the FIB with an inductively coupled plasma ion source (plasma-FIB) (e.g., Smith et al. 2014) and X-ray microscopy (XRM) or nano-CT (e.g., Gelb et al. 2011) will enable us to overcome sample size limitations and to characterize multi-scale hierarchical pore topology.

LB-BASED APPLICATIONS FOR PRECIPITATION, DISSOLUTION, AND BIOFILM GROWTH AND THEIR IMPACT ON FLOW ALTERATION

Pore cementation/dissolution and flow feedback

Here we summarize a few of LB-based works that emphasize coupling among fluid flow, reaction, and flow feedback. Kang and co-workers have applied an LB pore-scale reactive transport model to study heterogeneous chemical reactions in a simple pore geometry under a variety of conditions (Kang et al. 2002, 2006). For example, Kang et al. (2006) demonstrated that the competition between diffusive and advective transport can alter permeability during the dissolution of different sizes of fracture aperture. More recently, Kang et al. (2014) applied a reactive transport LB model to study the change of porosity and permeability due to dissolution over a wide range of Péclet (Pe , the ratio of advective to diffusive transport) and Damköhler (Da , the ratio of reaction rate to diffusive mass transfer rate) numbers. They demonstrated that the permeability-porosity relationship is affected by different dissolution regimes in terms of Pe and Da numbers, but also by the specific porous medium structure. In particular, the relationship for the more geometrically complex porous medium shows more complexity than that for the simple fractured medium (Fig. 9). For the complex medium, a combination of a high Pe and Da (i.e., fast-flow and fast-reaction regime) results in wormholing and exhibits the fastest permeability increase. At a moderate Pe and high Da , a transition from a transport-limited dissolution regime to wormholing is observed for the complex medium as shown in Figure 9. Huber et al. (2014) applied a newly developed LB model with a new boundary scheme for heterogeneous reactions to study the permeability change of a porous medium due to dissolution and precipitation. They highlighted that relative permeability changes differ under dissolution and precipitation regimes. The permeability changes during dissolution were controlled by both reaction and transport (as the transport regime transitions from diffusion to advection). Increases in permeability correlate positively with Pe , but negatively with Da for a given amount of porosity increase. On the other hand, increases in precipitation correlate negatively with Pe , but positively with Da . This behavior suggests the presence of a hysteresis in the permeability and porosity relationship during cycles of dissolution and precipitation.

Jiang and Tsuji (2014) developed a LB-FVM model for exploring the porosity and relative permeability changes caused by carbonate precipitation in 3-D digital microstructures obtained from micro-CT imaging of a Berea sandstone sample. Changes of pore structures caused by carbonate precipitation are shown in Figure 10. For the sake of simplification, chemical reactions in aqueous solution were assumed in equilibrium and only Ca^{2+} concentration was solved by the advection-diffusion model. All pore structures were assumed reactive surfaces for carbonate precipitation. The porosity was reduced from 0.21 to 0.103 after ~ 20 days of precipitation (Fig. 10). The porosity change corresponds to the reduction of permeability from 769 mD to 11 mD. In particular, simulations of multiphase flow in the altered pore structure demonstrated that reduced pore space (a final case in Figure 10) affects the relative permeability of the nonwetting phase more significantly than that of the wetting phase. This finding implies that mineralization may significantly impact the injectivity of CO_2 in water wetting conditions during geologic CO_2 storage.

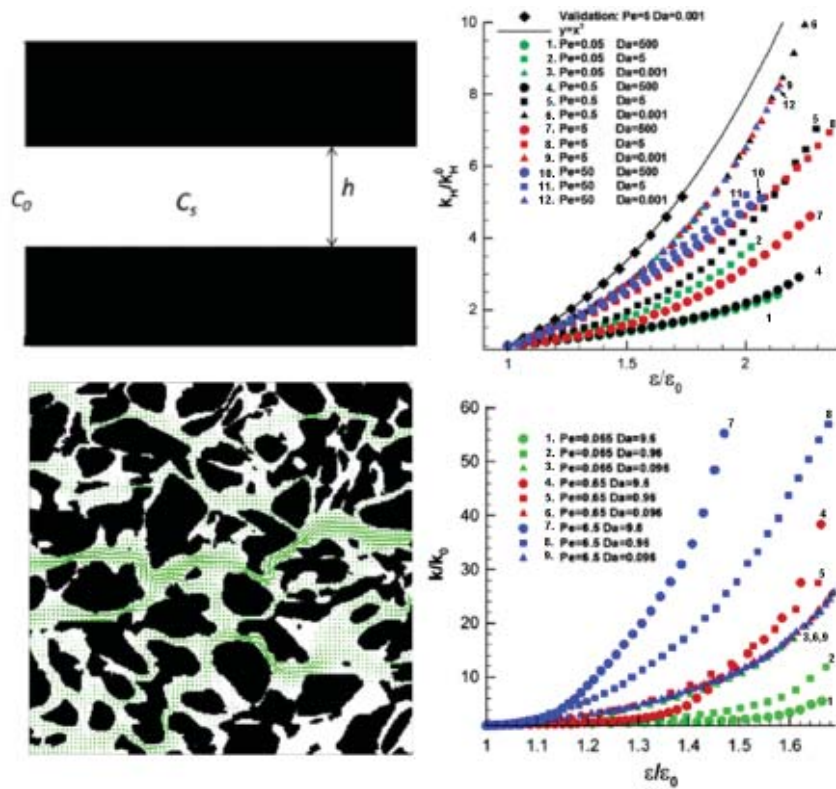


Figure 9. Two different porous medium structures (left) and corresponding permeability-positivity relationships (right) [Used by permission of Elsevier, from Kang Q, Chen L, Valocchi AJ, Viswanathan HS (2014) Pore-scale study of dissolution-induced changes in permeability and porosity of porous media. *Journal of Hydrology*, Vol. 517, Figures 1-4, p. 1051-1052].

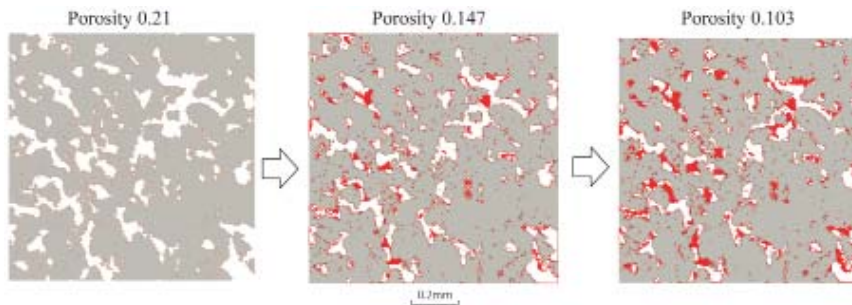


Figure 10. Evolution of pore structure resulting from CaCO_3 precipitation along a cross-sectional slice perpendicular to the main flow direction (light gray for original grain and dark red for precipitated regions). 3-D pore structure reconstructed from micro-CT images of a Berea sandstone was used [Used by permission of American Physical Society, from Jiang F, Tsuji T (2014) Changes in pore geometry and relative permeability caused by carbonate precipitation in porous media. *Physical Review E*, Vol. 90, Fig. 8, p. 053306-6].

Microfluidic experiments for pore cementation and flow blocking

Recent developments of *in situ* measurement techniques for pore-scale reactive transport experiments provide a unique opportunity to test and validate pore-scale modeling approaches. In particular, a coupled pore-scale reactive transport model was rigorously validated against well-controlled microfluidic experimental results to demonstrate the importance of realistic pore configurations, flow and transport physics and geochemistry, and to predict how mineral precipitation alters flow paths by pore plugging for different chemical conditions (Yoon et al. 2012; Fanizza et al. 2013; Boyd et al. 2014; Oostrom et al. 2014). The coupled model consists of LBM for fluid flow and FVM for reactive transport with mineral precipitation and dissolution. Heterogeneous reactions were solved using the boundary condition given by Equations (10–13). Pore-scale experiments led by Werth and co-workers (Zhang et al. 2010a; Fanizza et al. 2013; Boyd et al. 2014) were used. The micromodel consisted of a 2×1 cm pore network containing a pattern of cylindrical posts ($300 \mu\text{m}$ in diameter) with $180\text{-}\mu\text{m}$ pore spaces and $40\text{-}\mu\text{m}$ pore throats, a depth of $\sim 20\text{--}40 \mu\text{m}$, and a porosity of ~ 0.39 . The micromodel surface was treated thermally to have a thin layer ($\sim 100 \text{ nm}$'s) of silicon dioxide, mimicking natural materials. Representative experimental observations are shown in Figure 11.

Transverse mixing-induced mineral precipitation experiments were performed by injecting solutions containing reactants (e.g., Ca^{2+} , Mg^{2+} , UO_2^{2+} , CO_3^{2-} , PO_4^{3-}) through two separate inlets of a micromodel. The amount of mineral precipitation, snapshots of the morphology of precipitates, elemental analysis with Raman spectroscopy, and LSCM imaging and tracer tests

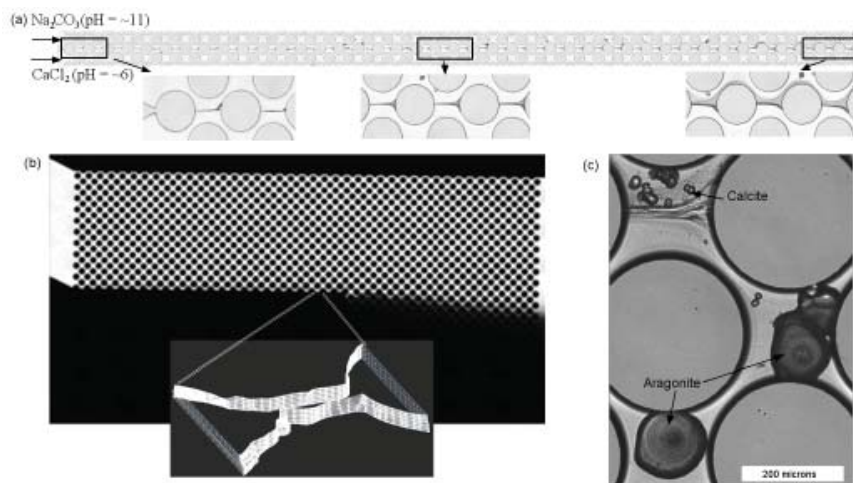


Figure 11. (a) A snapshot of calcium carbonate precipitation with 25mM Ca^{2+} (upper inlet) and 25mM CO_3^{2-} (bottom inlet). Precipitation patterns at three different locations are highlighted [Used by permission of John Wiley and Sons, from Yoon H, Valocchi AJ, Werth CJ, Dewers T (2012) Pore-scale simulation of mixing-induced calcium carbonate precipitation and dissolution in a microfluidic pore network. *Water Resources Research*, Vol. 48, Fig. 1, p. W02524-3]. (b) Tracer test result after pore blockage. A profile of 3-D precipitates halfway down the length of the micromodel was obtained using confocal microscope, showing a complete pore blockage over a $\sim 40 \mu\text{m}$ depth [Used by permission of John Wiley and Sons, from Fanizza MF, Yoon H, Zhang C, Oostrom M, Wietsma TW, Hess NJ, Bowden ME, Strathmann TJ, Finneran KT, Werth CJ (2013) Pore-scale evaluation of uranyl phosphate precipitation in a model groundwater system. *Water Resources Research*, Vol. 49, Figures 10–11, p. 886]. (c) Microscopy images of CaCO_3 polymorphs in the presence of 40 mM Mg^{2+} with 10mM Ca^{2+} (upper inlet) and 10mM CO_3^{2-} (bottom inlet). The central mixing line in the micrometer is shown in an upper-left pore body [Used by permission of Elsevier, from Boyd T, Yoon H, Zhang C, Dehoff K, Fouke B, Valocchi AJ, Werth CJ (2014) Influence of Mg^{2+} on CaCO_3 precipitation during subsurface reactive transport in a homogeneous silicon-etched pore network. *Geochimica et Cosmochimica Acta*, Vol. 135, Fig. 5, p. 329].

for pore blockage were measured. Specifically, the coupled LB–FVM approach for pore-scale reactive transport problems includes calcium carbonate precipitation and dissolution kinetics (Yoon et al. 2012), uranyl phosphate precipitation to account for reaction mechanisms under different chemical conditions (Fanizza et al. 2013), and the impact of magnesium on calcium carbonate precipitation (Boyd et al. 2014). In particular, tracer tests (e.g., Fig. 11b) indicate that mineral precipitation along the center mixing zone led to substantial pore blockage under all experimental conditions. The observed changes in crystal shape, size, polymorph, and precipitation rate under different chemical conditions suggest that proper chemistry systems be considered in determining the impact of pore blockage on mixing and reaction.

In Yoon et al. (2012) a chemical system for CaCO_3 precipitation and dissolution includes five primary components: Na^+ , Ca^{2+} , H^+ , CO_3^{2-} , and Cl^- , and a number of secondary species: OH^- , HCO_3^- , and H_2CO_3 (aq). Simulation results are shown in Figure 12. The reactive transport model included the impact of pH upon carbonate speciation and calcite dissolution using the form of the calcite rate law (Chou et al. 1989):

$$k_m = k_1 a_{\text{H}^+} + k_2 a_{\text{H}_2\text{CO}_3} + k_3, \quad (42)$$

where k_m is the reaction rate constant in Equation (10), k_1 , k_2 , and k_3 are the empirically obtained reaction rate constants, and a_i is the activity of species i . The calcite reaction rate is pH-dependent ($\text{pH} < 7$), but becomes constant above a pH of ~ 7.5 . A similar chemical system for CaCO_3 precipitation and dissolution in the flowing system was used in the literature (Emmanuel and Berkowitz 2005; Tartakovsky et al. 2008; Flukiger and Bernard 2009; Kang et al. 2010; Molins et al. 2012). In the above formulation, the key discrepancy between pore and continuum scales is the reactive surface area. As described earlier, heterogeneous reactions at mineral interfaces can be treated through the boundary conditions (Eqn. 11). In particular, Yoon et al. (2012) developed an algorithm to update a specific surface area over time in the micromodel, depending on the orientation of CaCO_3 growth and dissolution. Updating the surface area properly was critical to accounting for the overall reaction rates as shown in Figure 12a. Hence, the specific surface area was updated at each iteration step.

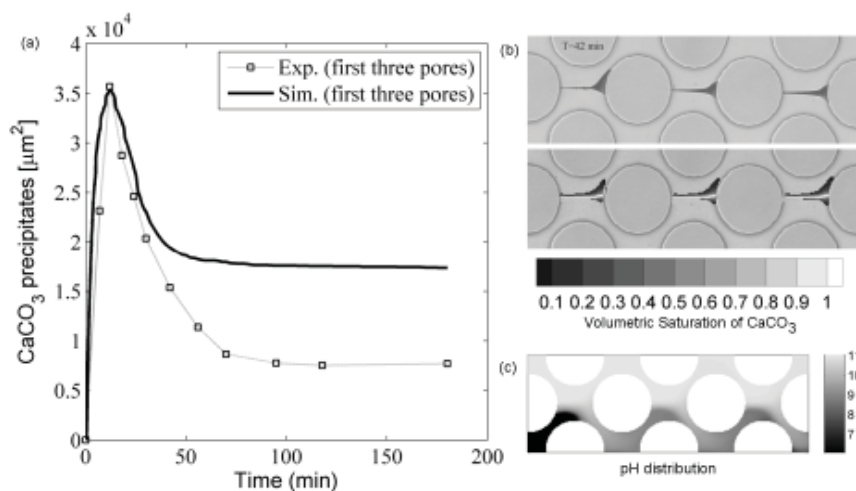


Figure 12. (a) Comparison of CaCO_3 precipitate areas, (b) experimental image of CaCO_3 precipitates (top), simulated CaCO_3 volumetric content (bottom), and (c) simulated pH distribution at 4 min [Used by permission of John Wiley and Sons, from Yoon H, Valocchi AJ, Werth CJ, Dewers T (2012) Pore-scale simulation of mixing-induced calcium carbonate precipitation and dissolution in a microfluidic pore network. *Water Resources Research*, Vol. 48, Figures 6–7, W02524-9].

It was also found that the proper estimation of the dissolution rate was necessary to adequately simulate the decrease of precipitate area (i.e., enhanced dissolution) after ~ 18 min. In this particular case, the dissolution rate increased by a factor of 100. Based on Raman spectroscopy and image analysis, a higher dissolution rate was attributed to stability of CaCO_3 polymorphs including amorphous calcium carbonate (ACC) and vaterite at early stages. ACC is the thermodynamically least stable among all calcium carbonate (CaCO_3) polymorphs, followed by vaterite, aragonite, and calcite. Under highly supersaturated conditions, ACC nanoparticles with a size of ~ 30 nm are formed within a minute; subsequently, these particles grow and transform with time to more stable crystalline forms such as vaterite crystals (Pouget et al. 2009; Liu et al. 2010), and eventually calcite (Ogino et al. 1987; Rieger et al. 2007). These polymorphs became unstable once the central part of pore body was blocked by precipitates, and then may have dissolved and re-precipitated under flowing condition. Unlike static conditions, dissolved components can be transported away in the flowing conditions, which can enhance dissolution rate dramatically. In addition, the surface features (e.g., pits) at nano-scale may enhance the dissolution. It was later computed that under highly supersaturated conditions used in the experiment the saturation ratio of ACC is greater than unity (Boyd et al. 2014), indicating that initial precipitation is likely to be initiated through homogeneous nucleation.

The coupled pore-scale reactive transport model was also used to account for the observed CO_2 seeps at the Grand Wash Fault field site (Crystal Geyser, Utah), a natural analog to geologic CO_2 sequestration (Altman et al. 2014). Field observations along the Grand Wash fault suggest that CaCO_3 precipitation alters flow paths by fault zone cementation, resulting in shifts in preferential flow paths of the upward migrating CO_2 -saturated-brine. Pore blocking was observed to be faster in a fracture near the main fault and propagated further away from the main fault, which qualitatively reflects the observed pattern at the Grand Wash Fault. This demonstrates that inclusion of more realistic pore configurations and geochemical composition may enhance our fundamental mechanistic explanations of how calcite precipitation alters flow paths by pore plugging.

Example results illustrating feedback between flow and biofilms

The pore-scale biofilm models have been used to investigate several important processes in porous media, including clogging and contaminant transformation, microbially-induced calcium carbonate precipitation (MICP), and bioengineering. We summarize a few of the many interesting works that emphasize coupling among fluid flow, mass transfer, and biofilm growth. For practical applications, bioclogging has been studied for many years using small porous medium reactors in the laboratory where it is generally only possible to observe bulk changes in permeability and other macroscopic properties (Vandevivere and Baveye 1992; Seifert and Engesgaard 2012). However, most pore-scale modeling studies of bioclogging have been in 2-D. Recently, von der Schulenburg et al. (2009) have conducted LB simulations in a 3-D bead packing. The porous medium geometry is derived from images taken by magnetic resonance imaging of saturated packing of random glass beads with mean diameter 400 μm and overall porosity 0.59. The biofilm develops over time, substrate is consumed, and the heterogeneity of the velocity field increases. The LB simulation results show that the computed permeability was smaller than the value computed from a commonly used correlation equation (i.e., the Ergun equation). Comparison of 2-D and 3-D simulations revealed that 3-D simulation is required to accurately model bioclogging.

Pintelon et al. (2012) extended the work of von der Schulenburg et al. (2009) by including biofilm detachment and allowing water flow through the biofilm to investigate the impact of biofilm permeability and strength upon macroscopic properties such as the Da number and permeability. The level-set method of Pintelon et al. (2009) was used to include shear induced detachment. Biofilm permeability was included by setting the fluid viscosity within

the biofilm to a high value, similar to the approach used by Thullner and Baveye (2008) in their pore network model. MRT-LBM was used to solve for the flow, and the different viscosity values for the fluid and biofilm nodes were achieved by adjusting the relaxation rates. A 3-D bead pack porous medium is considered, similar to that of von der Schulenburg et al. (2009). Results from a 2-D slice transverse to the mean flow direction are shown in Figure 13. The top row is for a biofilm with high material strength while the bottom is for a weak biofilm. The parameter X equals the viscosity ratio of the biofilm to fluid cells, so from left to right the biofilm region is more permeable to water flow. The biofilm with the weaker cohesive strength has significantly less overall accumulation than the stronger biofilm; biofilm permeability has a secondary influence because fluid shear stress is smaller for the more permeable biofilm. The permeability reduces over time as the biomass accumulates. It was observed that the biofilm permeability needs to be relatively high (low X) before there is a significant impact upon the overall permeability of the system.

Unlike the cases reported above with a single limiting substrate, biofilms can develop in the situation where separately flowing electron donors and acceptors meet and mix. This situation can occur during *in situ* bioremediation along the fringes of a contaminant plume from a persistent source where oxygen present in the ambient groundwater mixes with a dissolved organic pollutant resulting in a “reaction zone” with biomass along the plume fringe (e.g., Cirpka and Valocchi 2007; Valocchi 2012). Werth and co-workers (Zhang et al. 2010b; Yoon et al. 2014) have used 2-D microfluidic pore networks to investigate these transverse reaction processes experimentally as described in the precipitation section. The electron donor and acceptor were injected through two separate inlets, allowing two substrates to mix around the central mixing zone. Initially, a pure bacterial strain was inoculated and the resulting biofilm developed along the mixing zone where both substrates are present. Following the experiments

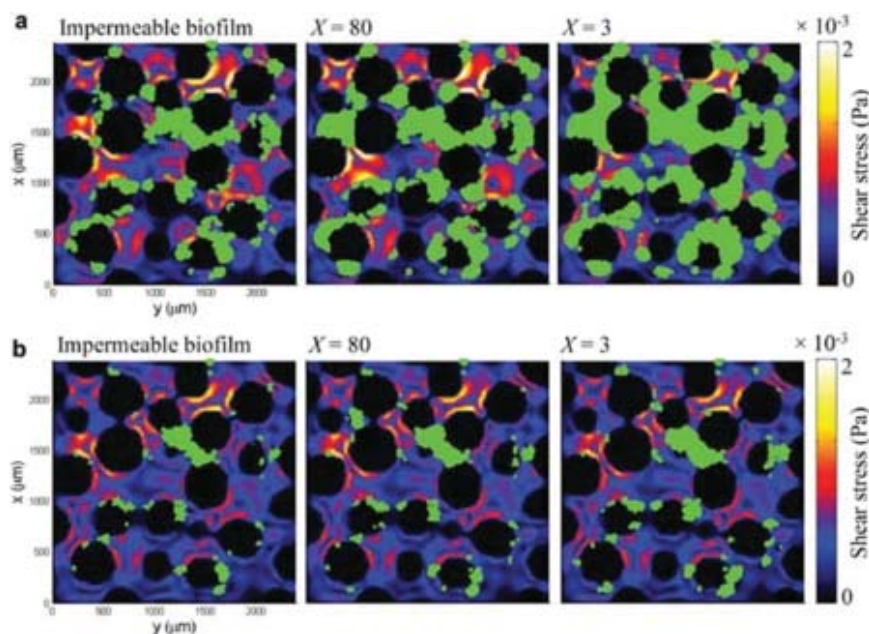


Figure 13. 2-D slice from the 3-D model results of Pintelon et al. (2012). Biomass is shown in green along with the shear stress field after 27 h of growth. Left panel is for an impermeable biofilm, and the biofilm permeability increases from left to right. Biomass was allowed to detach depending on adjacent shear stresses; the top row is a comparatively strong biofilm, while the bottom row is a comparatively weak biofilm. As the parameter X decreases, the biofilm permeability increases. [Used by permission of John Wiley and Sons, from Fredrich JT, DiGiovanni AA, Noble DR (2006) Predicting macroscopic transport properties using microscopic image data. *Journal of Geophysical Research*, Vol. 111, Fig. 7, B03201-10].

in Zhang et al. (2010b) where the biofilm developed with the aerobic degradation of the herbicide (i.e., R-2,4-DP), Yoon et al. (2014) introduced another substrate to induce adaptation of the strain to degrade a new substance on which an unadapted strain is not able to grow. Over a long term operation (~ 230 days), relatively thick and sturdy biofilm was developed along the mixing line. Due to the presence of thick and non-uniform biofilm, transverse mixing increased dramatically, which was also significantly affected by flowrates.

Tang et al. (2013) developed a 2-D pore-scale model that uses LB-FDM for the flow field and the advection–diffusion–reaction equations (with dual Monod kinetics), and the CA model for biofilm spreading. There was a good qualitative comparison between the growth pattern in the model and micromodel experiment, for a close up of the system in the mixing zone (Fig. 14). The biofilm develops along the downstream side of the cylindrical post and extends out into the pore body. It is important to note that the model biofilm would completely bridge the pore body unless the CA rules are modified to prevent biomass spreading to zones with fluid shear above a certain threshold (Knutson et al. 2005). In the model of Tang et al. (2013), the biomass is assumed to be impermeable, and hence the growing biofilm reduces the velocity in the mixing zone which results in decreased transverse mixing between the donor and acceptor (Fig. 14). The importance of this effect was further evaluated by repeating their simulations using the velocity field computed without any biomass. They then computed the mass of donor degraded from the inlet to the outlet and compared that to what was measured in the experiment. The results clearly show that the feedback among biofilm growth, velocity alteration, and mass transfer is important. Neglecting the dynamic changes in the pore space and instead using a constant velocity results in an overestimation of mixing and overall reaction.

There is an increasing knowledge about the mechanical properties of biofilms, which will lead to more complete and accurate models of attachment and detachment processes. Although several groups have incorporated some of these processes into discrete CA or IB models of biofilms (e.g., Pintelon et al. 2012 ; Bottero et al. 2013), physics-based models using

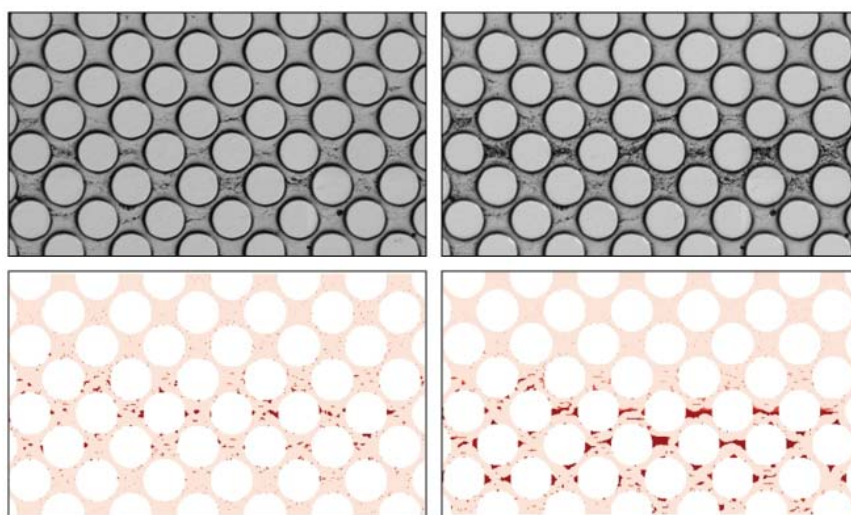


Figure 14. Comparison of the biofilm spreading in the experiment (top) of Zhang et al. (2010b) with the model results (bottom) by Tang et al. (2013) after 11 days (left) and 24 days (right). [Top: Used by permission of American Chemical Society, from Zhang C, Kang Q, Wang X, Zilles JL, Müller RH, Werth CJ (2010b) Effects of pore-scale heterogeneity and transverse mixing on bacterial growth in porous media. *Environmental Science & Technology*, Vol. 44, Fig. 3, p. 3088; Bottom: Used by permission of John Wiley and Sons, from Tang Y, Valocchi AJ, Werth CJ, Liu H (2013) An improved pore-scale biofilm model and comparison with a microfluidic flow cell experiment. *Water Resources Research*, Vol. 111, Fig. 6, p. 8376].

mixture theory (e.g., Lindley et al. 2012) or dissipative particle dynamics (Xu et al. 2011) may be more flexible. These more complete mechanical models could address the transport and possible re-attachment of biomass that detaches from upstream.

FUTURE RESEARCH DIRECTIONS

We have summarized LBM models for fluid flow and reactive transport processes involving pore structure evolution and flow feedback due to mineral precipitation and dissolution and biofilm dynamics. In particular, recent algorithms for heterogeneous reactions and biofilm growth at mineral surfaces were thoroughly reviewed. Several key hybrid approaches combining LB with other methods were briefly introduced. Due to the growing body of literature over diverse disciplines, many ongoing research areas are only briefly cited and summarized. Despite the significant amount of works, upscaling coupled pore-scale phenomena including heterogeneous biogeochemical reactions, chemical–mechanical–hydrological coupling, and links between pore- and continuum-scale rates are still frontier research questions.

Recent progress in imaging, experimental and computing technologies has resulted in an increased adoption of digital visualization or direct measurement methods in pore-scale reactive transport studies. Using multi-scale imaging methods, we are now able to directly measure how surface chemistry, biogeochemical reactions, and pore topology impact reactive transport processes at the pore scale. Likewise, recent increases in parallel computing and computational methods allow us to simulate reactive transport processes in great detail. For example, it will be possible within the near future to simulate reactive transport experiments directly on the reconstructed 3-D image of porous and fractured media from nano to core scales. Although we focused on reviewing flow and reactive transport processes under saturated conditions, unsaturated porous media have also been recently studied (e.g., Raof 2011; Yang et al. 2014a). Coupled pore-scale flow and reactive transport under variably saturated conditions will be an important future research area due to its significance for soil biogeochemical processes in terrestrial systems for carbon cycle and the interaction between hydrological and biogeochemical processes for water and mass fluxes.

Many of the important engineering challenges that motivate the study of biofilms in porous media (e.g., bioclogging, microbial enhanced oil recovery, bioremediation) involve coupled biotic and abiotic processes. For example, injection of electron donors for biostimulation to reduce dissolved metals in groundwater at some US DOE facilities can require modeling a complex network of biotic and abiotic reactions (e.g., Scheibe et al. 2006). However, pore-scale modeling has been limited because there are conceptual and mathematical challenges for modeling simultaneous biofilm spreading and mineral precipitation. A recent attempt by Zhang and Klapper (2014) using the phase-field model is an encouraging sign of developing a pore-scale model for coupled biotic and abiotic processes. Some researchers have begun to explore so-called *in silico* models of microbial metabolism based on genomic knowledge instead of the phenomenological Monod model for substrate utilization (e.g., Fang et al. 2011) and to incorporate microbial motility characteristics into cell-scale and porous media models (e.g., Kusy and Ford 2007). Inclusion of more realistic microbial phenomena in pore-scale biofilm models will significantly improve model predictions of coupled biotic and abiotic processes.

The LB-based approaches and experimental and numerical results reviewed in this article are leading to better understanding of complex problems of evolving pore morphology due to tightly coupled transport and nonlinear reactions. However, the ultimate goal is to improve predictive capability at larger continuum and field scales. As conventional homogenization and volume-averaging techniques are not valid due to process nonlinearity and the lack of scale separation, pore-scale modeling is enabling new methods of upscaling, including multi-

scale, multi-physics approaches (Chu et al. 2013; Tomin and Lunati 2013; Varloteaux et al. 2013; Scheibe et al. 2015). A key assumption of the methods reviewed here is that all processes as well as the pore geometry can be quantified unambiguously at the smallest scale (i.e., pore scale). There are new emerging problems (e.g., unconventional resources in shale and carbonate rocks, caprock for CO₂ sequestration) for which it may be necessary to model key processes at the nanometer scale, but the practical scale of observation is generally limited to a micro-scale (10's–100's microns). New approaches based on mesoscopic theories, which connect the microscopic and macroscopic descriptions of the dynamics, provide a promising outcome (DOE 2012). Key relationships and parameter values at the macroscopic scale can be constructed from microscopic-scale simulations including sub-micron scale, which account for a range of reaction and flux regimes. For such problems, the LB-based modeling framework reviewed in this article as well as other multiscale simulation methods can help us improve our understanding of reactive transport processes by elucidating knowledge gaps and providing a tool in predicting coupling relevant processes across scales.

ACKNOWLEDGMENTS

Work by HY on the entire manuscript was supported as part of the Center for Frontiers of Subsurface Energy Security, an Energy Frontier Research Center funded by the U.S. Department of Energy, Office of Science, Office of Basic Energy Sciences under Award Number DE-SC0001114. Sandia National Laboratories is a multi-program laboratory managed and operated by Sandia Corporation, a wholly owned subsidiary of Lockheed Martin Corporation, for the U.S. Department of Energy's National Nuclear Security Administration under contract DE-AC04-94AL85000. QK acknowledges Los Alamos National Laboratory's Laboratory Directed Research and Development Program and Institutional Computing Program. AJV acknowledges support for biofilm applications from the U.S. Department of Energy Subsurface Biogeochemistry Research Program under Award No. DE-SC0006771. Additional work by AJV on mineral precipitation applications was supported as part of the Center for Geologic Storage of CO₂, an Energy Frontier Research Center funded by the U.S. Department of Energy, Office of Science, Office of Basic Energy Sciences under Award Number DOE DE-SC0012504. AJV also would like to thank Dr. Youneng Tang for assistance surveying the literature and for his insights on biofilm modeling. HY would like to thank Peter Mozley for providing images in Figure 1. We also acknowledge the effort of Carl Steefel, Sergi Molins, and Simon Emmanuel for their careful and constructive reviews, which led to significant improvement of our chapter.

REFERENCES

- Adkins JP, Tanner RS, Udegbunam EO, Mcinerney MJ, Knapp RM (1992) Microbially enhanced oil recovery from unconsolidated limestone cores. *Geomicrobiol J* 10:77–86
- Alpkvist E, Klapper I (2007) A multidimensional multispecies continuum model for heterogeneous biofilm development. *Bull Math Biol* 69:765–789
- Altman SJ, Aminzadeh B, Balhoff MT, Bennett PC, Bryant SL, Cardenas MB, Chaudhary K, Cygan RT, Deng W, Dewers T, DiCarlo DA, Eichhubl P, Hesse MA, Huh C, Matteo EN, Mehmani Y, Tenney CM, Yoon H (2014) Chemical and hydrodynamic mechanisms for long-term geological carbon storage. *J Phys Chem C* 118:15103–15113
- Andrá H, Combaret N, Dvorkin J, Glatt E, Han J, Kabel M, Keehm Y, Krzikalla F, Lee M, Madonna C, Marsh M, Mukerjic T, Saenger EH, Sain R, Saxena N, Ricker S, Wiegmann A, Zhan X (2013a) Digital rock physics benchmarks-Part I: Imaging and segmentation. *Comput Geosci* 50:25–32
- Andrá H, Combaret N, Dvorkin J, Glatt E, Han J, Kabel M, Keehm Y, Krzikalla F, Lee M, Madonna C, Marsh M, Mukerjic T, Saenger EH, Sain R, Saxena N, Ricker S, Wiegmann A, Zhan X (2013b) Digital rock physics benchmarks-Part II: Computing effective properties. *Comput Geosci* 50:33–43

- Arns CH, Knackstedt MA, Pinczewski WV, Garboczi EJ (2002) Computation of linear elastic properties from microtomographic images: methodology and agreement between theory and experiment. *Geophys* 67:1395–1405
- Arns CH, Knackstedt MA, Mecke KR (2009) Boolean reconstructions of complex materials: Integral geometric approach. *Phys Rev E* 80:051303
- Baldessari F (2008) Electrokinetics in nanochannels - Part I. Electric double layer overlap and channel-to-well equilibrium. *J Colloid Interfac Sci* 325:526–538
- Bancroft WD (1926) *Applied Colloid Chemistry General Theory*. McGraw-Hill, New York
- Battiato I, Tartakovsky DM, Tartakovsky AM, Scheibe TD (2011) Hybrid models of reactive transport in porous and fractured media. *Adv Water Resour* 37:1140–1150
- Bhatnagar PL, Gross EP, Krook M (1954) A model for collision processes in gases. I. small amplitude processes in charged and neutral one-component systems. *Phys Rev* 94:511–525
- Bilger N, Auslender F, Bornert M, Michel JC, Moulinec H, Suquet P, Zaoui A (2005) Effect of a nonuniform distribution of voids on the plastic response of voided materials: a computational and statistical analysis. *Int J Solids Struct* 42:517–538
- Boek ES, Zacharoudiou I, Gray F, Shah SMK, Crawshaw J, Yang J (2014) Multiphase flow and reactive transport at the pore scale using lattice-Boltzmann computer simulations. SPE-170941-MS, SPE Annual Technical Conference and Exhibition, Society of Petroleum Engineers
- Bottero S, Storck T, Heimovaara TJ, van Loosdrecht MCM, Enzien MV, Picioreanu C (2013) Biofilm development and the dynamics of preferential flow paths in porous media. *Biofouling* 29:1069–1086
- Bouzidi MH, Firdaouss M, Lallemand P (2001) Momentum transfer of a Boltzmann-lattice fluid with boundaries. *Phys Fluids* (1994–present) 13:3452–3459
- Boyd T, Yoon H, Zhang C, Dehoff K, Fouke B, Valocchi AJ, Werth CJ (2014) Influence of Mg^{2+} on $CaCO_3$ precipitation during subsurface reactive transport in a homogeneous silicon-etched pore network. *Geochim Cosmochim Acta* 135:321–335
- Breyers J (1988) Modeling biofilm accumulation. *In: Physiology Models in Microbiology*. Bazin MJ, Prosser JI (eds) CRC Press, Boca Raton FL, p 109–144
- Chen LQ (2002) Phase-filed models for microstructures evolution. *Ann Rev Mater Res* 32:113–140
- Chen S, Doolen G (1998) Lattice Boltzmann method for fluid flows. *Ann Rev Fluid Mech* 30:329–364
- Chen S, He X, Luo LS (2007) Lattice Boltzmann models for multiphase flows. *In: Computational Methods for Multiphase Flow*. Prosperetti A, Tryggvason G (eds) Cambridge University Press, p 157–192, <http://dx.doi.org/10.1017/CBO9780511607486.007>
- Chen L, Kang Q, He YL, Tao WQ (2012) Mesoscopic study of the effect of gel concentration and material on the formation of precipitation patterns. *Langmuir* 28:11745–11754
- Chen L, He YL, Kang Q, Tao WQ (2013a) Coupled numerical approach combining finite volume and lattice Boltzmann methods for multi-scale multi-physicochemical processes. *J Comput Phys* 255:83–105
- Chen L, Kang Q, Robinson BA, He YL, Tao WQ (2013b) Pore-scale modeling of multiphase reactive transport with phase transitions and dissolution-precipitation processes in closed systems. *Phys Rev E* 87:043306
- Chen L, Kang Q, Carey B, Tao WQ (2014a) Pore-scale study of diffusion–reaction processes involving dissolution and precipitation using the lattice Boltzmann method. *Int J Heat Mass Transf* 75:483–496
- Chen L, Kang Q, Viswanathan HS, Tao WQ (2014b) Pore-scale study of dissolution-induced changes in hydrologic properties of rocks with binary minerals. *Water Resour Res* 50:9343–9365, doi:10.1002/2014WR015646
- Chou L, Garrels RM, Wollast R (1989) Comparative study of the kinetics and mechanisms of dissolution of carbonate minerals. *Chem Geol* 78:269–282
- Chu J, Engquist B, Prodanovič M, Tsai R (2013) A multiscale method coupling network and continuum models in porous media II—Single-and two-phase flows. *In: Advances in Applied Mathematics, Modeling, and Computational Science*. Melnik R, Kotsireas IS (eds) Springer US, p 161–185
- Cirpka OA, Valocchi AJ (2007) Two-dimensional concentration distribution for mixing-controlled bioreactive transport in steady state. *Adv Water Resour* 30:1668–1679
- Coker DA, Torquato S, Dunsmuir JH (1996) Morphology and physical properties of Fontainebleau sandstone via a tomographic analysis. *J Geophys Res: Solid Earth* (1978–2012) 101(B8):17497–17506
- Coles ME, Hazlett RD, Spanne P, Soll WE, Muegge EL, Jones KW (1998) Pore level imaging of fluid transport using synchrotron X-ray microtomography. *J Petrol Sci Eng* 19:55–63
- d’Humières D, Ginzburg I, Krafczyk M, Lallemand P, Luo LS (2002) Multiple–relaxation–time lattice Boltzmann models in three dimensions. *Philosophical Transactions of the Royal Society of London. Series A: Mathematical, Physical and Engineering Sciences* 360:437–451
- Davery ME, Gevertz D, Wood WA, Clark JB, Jenneman GE (1998) Microbial selective plugging of sandstone through stimulation of indigenous bacteria in a hypersaline oil reservoir. *Geomicrobiol J* 15:335–352
- Davidson SM, Yoon H, Martinez MJ (2012) Pore scale analysis of the impact of mixing-induced reaction on viscosity variations. *Adv Water Resour* 38:70–80

- Dawson SP, Chen S, Doolen GD (1993) Lattice Boltzmann computations for reaction-diffusion equations. *J Chem Phys* 98:1514–1523
- DeJong J, Fritzges M, Nüsslein K (2006) Microbially induced cementation to control sand response to undrained shear. *J Geotech Geoenv Eng* 132:1381–1392
- Deng W, Cardenas MB, Kirk MF, Altman SJ, Bennett PC (2013) Effect of Permeable Biofilm on Micro-And Macro-Scale Flow and Transport in Bioclogged Pores. *Env Sci Techol* 47:11092–11098
- DOE (2007) Basic Research Needs for Geosciences: Facilitating 21st Century Energy Systems. A report from the Workshop Sponsored by the US Department of Energy, Office of Basic Energy Sciences, Bethesda, MA, Feb. 21-23, 2007
- DOE (2012) From Quanta to the Continuum: Opportunities for Mesoscale Science. A report from the Basic Energy Sciences Advisory Committee, US Department of Energy, Office of Basic Energy Sciences, September, 2012
- Dupin HJ, Kitanidis PK, McCarty PL (2001) Pore-scale modeling of biological clogging due to aggregate expansion: A material mechanics approach. *Water Resour Res* 37:2965–2979
- El Mountassir G, Lunn RJ, Moir H, MacLachlan E (2014) Hydrodynamic coupling in microbially mediated fracture mineralization: Formation of self-organized groundwater flow channels. *Water Resour Res* 50:1–16, doi:10.1002/2013WR013578
- Emmanuel S, Berkowitz B (2005) Mixing-induced precipitation and porosity evolution in porous media. *Adv Water Resour* 28:337–344
- Fang Y, Scheibe TD, Mahadevan R, Garg S, Long PE, Lovley DR (2011) Direct coupling of a genome-scale microbial in silico model and a groundwater reactive transport model. *J Contam Hydrol* 122:96–103
- Fanizza MF, Yoon H, Zhang C, Oostrom M, Wietsma TW, Hess NJ, Bowden ME, Strathmann TJ, Finneran KT, Werth CJ (2013) Pore-scale evaluation of uranyl phosphate precipitation in a model groundwater system. *Water Resour Res* 49:874–890
- Flukiger F, Bernard D (2009) A new numerical model for pore scale dissolution of calcite due to CO₂ saturated water flow in 3D realistic geometry: Principles and first results. *Chem Geol* 265:171–180
- Fredrich JT, Menendez B, Wong TF (1995) Imaging the pore structure of geomaterials. *Science* 268(5208):276–279
- Fredrich JT, DiGiovanni AA, Noble DR (2006) Predicting macroscopic transport properties using microscopic image data. *J Geophys Res* 111:B03201, doi: 10.1029/2005JB003774
- Fu LM, Lin JY, Yang RJ (2003) Analysis of electroosmotic flow with step change in zeta potential. *J Colloid Interfac Sci* 258:266–275
- Gao J, Xing H, Rudolph V, Li Q, Golding SD (2015) Parallel lattice Boltzmann computing and applications in core sample feature evaluation. *Transp Porous Media* 107:65–77
- Gelb J, Gu A, Fong T, Hunter L, Lau SH, Yun W (2011) A closer look at shale: Representative elementary volume analysis with laboratory 3D X-Ray computed microtomography and nanotomography. SCA2011-58. The International Symposium of the Society of Core Analysts, Austin, Texas, USA, September 18–21, 2011
- Ginzburg I, d’Humières D (2003) Multireflection boundary conditions for lattice Boltzmann models. *Phys Rev E* 68:066614
- Golfier F, Wood BD, Orgogozo L, Quintard M, Buès M (2009) Biofilms in porous media: Development of macroscopic transport equations via volume averaging with closure for local mass equilibrium conditions. *Adv Water Resour* 32:463–485
- Groen D, Hetherington J, Carver HB, Nash RW, Bernabeu MO, Coveney PV (2013) Analysing and modelling the performance of the HemeLB lattice-Boltzmann simulation environment. *J Comput Sci* 4:412–422
- Gualda GA, Baker DR, Polacci M (2010) Introduction: Advances in 3D imaging and analysis of geomaterials. *Geosphere* 6:468–469
- Guo ZL, Zhao TS, Shi Y (2005) A lattice Boltzmann algorithm for electro-osmotic flows in microfluidic devices. *J Chem Phys* 122:144907
- Harvey RW, Garabedian SP (1991) Use of colloid filtration theory in modeling movement of bacteria through a contaminated sandy aquifer. *Environ Sci Technol* 25:178–185
- He X, Li N (2000) Lattice Boltzmann simulation of electrochemical systems. *Comput Phys Commun* 129:158–166
- He X, Zou Q, Luo LS, Dembo M (1997) Analytic solutions of simple flows and analysis of nonslip boundary conditions for the lattice Boltzmann BGK model. *J Stat Phys* 87:115–136
- Hilpert M (2005) Lattice-Boltzmann model for bacterial chemotaxis. *J Math Biol* 51:302–332
- Hilpert M (2011) Determination of dimensional flow fields in hydrogeological settings via the MRT lattice-Boltzmann method. *Water Resour Res* 47:W09508, doi:10.1029/2010WR010016
- Hiorth A, Jettestuen E, Cathles L, Madland M (2013) Precipitation, dissolution, and ion exchange processes coupled with a lattice Boltzmann advection diffusion solver. *Geochim Cosmochim Acta* 104:99–110

- Holst M, Baker N, Wang F (2000) Adaptive multilevel finite element solution of the Poisson–Boltzmann equation I. Algorithms and examples. *J Comput Chem* 21:1319–1342
- Huber C, Parmigiani A, Chopard B, Manga M, Bachmann O (2008) Lattice Boltzmann model for melting with natural convection. *Int J Heat Fluid Fl* 29:1469–1480
- Huber C, Shafei B, Parmigiani A (2014) A new pore-scale model for linear and non-linear heterogeneous dissolution and precipitation. *Geochim Cosmochim Acta* 124:109–130
- IWA Task Group on Biofilm Modeling (2006) *Mathematical Modeling of Biofilms*. IWA Publishing, Hove, UK
- Jiang F, Tsuji T (2014) Changes in pore geometry and relative permeability caused by carbonate precipitation in porous media. *Phys Rev E* 90:053306
- Joshi AS, Sun Y (2009) Multiphase lattice Boltzmann method for particle suspensions. *Phys Rev E* 79:066703
- Kang QJ, Lichtner PC (2013) A lattice Boltzmann method for coupled fluid flow, solute transport, and chemical reaction. *In: Progress in Computational Physics*. Ehrhardt M (ed) Bentham Science Publishers
- Kang S, Suh YK (2006) Unsteady electroosmotic channel flows with the nonoverlapped and overlapped electric double layers. *J Mech Sci Technol* 20:2250–2264
- Kang QJ, Zhang DX, Chen SY, He XY (2002) Lattice Boltzmann simulation of chemical dissolution in porous media. *Phys Rev E* 65:036318
- Kang Q, Zhang D, Chen S (2003) Simulation of dissolution and precipitation in porous media. *J Geophys Res* 108(B10):2505
- Kang Q, Zhang D, Lichtner PC, Tsimpanogiannis IN (2004) Lattice Boltzmann model for crystal growth from supersaturated solution. *Geophys Res Lett* 31:L21604
- Kang QJ, Lichtner PC, Zhang DX (2006) Lattice Boltzmann pore-scale model for multicomponent reactive transport in porous media. *J Geophys Res-Solid Earth* 111:B05203, doi:10.1029/2005JB003951
- Kang Q, Lichtner PC, Zhang D (2007) An improved lattice Boltzmann model for multicomponent reactive transport in porous media at the pore scale. *Water Resour Res* 43:W12S14
- Kang Q, Lichtner P, Viswanathan H, Abdel-Fattah A (2010) Pore scale modeling of reactive transport involved in geologic CO₂ sequestration. *Transp Porous Media* 82:197–213
- Kang Q, Chen L, Valocchi AJ, Viswanathan HS (2014) Pore-scale study of dissolution-induced changes in permeability and porosity of porous media. *J Hydrol* 517:1049–1055
- Karniadakis G, Beskok A, Aluru N (2005) *Microflows and Nanoflows: Fundamentals and Simulation*. Springer, New York.
- Keehm Y, Mukerji T, Nur A (2004) Permeability prediction from thin sections: 3D reconstruction and Lattice-Boltzmann flow simulation. *Geophys Res Lett* 31:L04606, doi:10.1029/2003GL018761
- Kelemen PB, Whitehead JA, Aharonov E, Jordahl KA (1995) Experiments on flow focusing in soluble porous media, with applications to melt extraction from the mantle. *J Geophys Res: Solid Earth* 100(B1):475–496
- Kim D, Peters CA, Lindquist WB (2011) Upscaling geochemical reaction rates accompanying acidic CO₂-saturated brine flow in sandstone aquifers. *Water Resour Res* 47:W01505, doi:10.1029/2010WR009472
- Kingdon RD, Schofield P (1992) A reaction-flow lattice Boltzmann model. *J Phys A* 25:L907–L910
- Kirk MF, Santillan EF, McGrath LK, Altman SJ (2012) Variation in hydraulic conductivity with decreasing pH in a biologically-clogged porous medium. *Int J Greenhouse Gas Control* 11:133–140
- Klapper I, Dockery J (2010) Mathematical description of microbial biofilms. *SIAM Review* 52:221–265
- Knutson CE, Werth CJ, Valocchi AJ (2005) Pore-scale simulation of biomass growth along the transverse mixing zone of a model two-dimensional porous medium. *Water Resour Res* 41:W07007, doi:10.1029/2004WR003459
- Kreft JU, Picioreanu C, Wimpenny JWT, van Loosdrecht MCM (2001) Individual-based modelling of biofilms. *Microbiol* 147:2897–2912
- Kusy K, Ford RM (2007) Monte Carlo simulations derived from direct observations of individual bacteria inform macroscopic migration models at granular porous media interfaces. *Env Sci Tech* 41:6403–6409
- Ladd AJ (1994) Numerical simulations of particulate suspensions via a discretized Boltzmann equation. Part I. Theoretical foundation. *J Fluid Mech* 271:285–309
- Landrot G, Ajo-Franklin JB, Yang L, Cabrini S, Steefel CI (2012) Measurement of accessible reactive surface area in a sandstone, with application to CO₂ mineralization. *Chem Geol* 318–319:113–125
- Lasaga AC (1981) Transition state theory. *Rev Mineral* 8:135–168
- Lasaga A (1998) *Kinetic Theory in the Earth Sciences*. Princeton Series in Geochemistry. Princeton University Press
- Lattice Boltzmann methods (2015, February 14). In Wikipedia, The Free Encyclopedia. http://en.wikipedia.org/w/index.php?title=Lattice_Boltzmann_methods&oldid=647112117
- Levich VG (1962) *Physico-Chemical Hydrodynamics*. Prentice-Hall, New York
- Li DQ (2001) Electro-viscous effects on pressure-driven liquid flow in microchannels. *Colloids and Surfaces A-Physicochemical and Engineering Aspects* 195:35–57
- Li DQ (2004) *Electrokinetics in Microfluidics*. Academic, Oxford

- Li L, Peters CA, Celia MA (2006) Upscaling geochemical reaction rates using pore-scale network modeling. *Adv Water Res* 29:1351–1370
- Li L, Peters CA, Celia MA (2007) Reply to “Comment on upscaling geochemical reaction rates using pore-scale network modeling” by Lichtner PC and Kang Q. *Adv Water Resour* 30:691–695
- Li X, Huang H, Meakin P (2008) Level set simulation of coupled advection-diffusion and pore structure evolution due to mineral precipitation in porous media. *Water Resour Res* 44:W12407
- Lichtner PC (1985) Continuum model for simultaneous chemical reactions and mass transport in hydrothermal systems. *Geochim Cosmochim Acta* 49:779–800
- Lichtner PC (1996) Continuum formulation of multicomponent-multiphase reactive transport. *Rev Mineral* 34:1–81
- Lichtner PC and Kang Q (2007) Comment on: “Upscaling geochemical reaction rates using pore-scale network modeling” by Li, Peters and Celia. *Adv Water Resour* 30:686–690
- Lichtner PC, Hammond GE, Lu C, Karra S, Bisht G, Andre B, Mills RT, Kumar J (2014) PFLOTRAN User Manual
- Lindley B, Wang Q, Zhang T (2012) Multicomponent hydrodynamic model for heterogeneous biofilms: Two-dimensional numerical simulations of growth and interaction with flows. *Phys Rev E* 85:031908
- LinkMasliyeh JH (2006). *Electrokinetic and Colloid Transport Phenomena*. Wiley-Interscience, Hoboken
- Liu J, Pancera S, Boyko V, Shukla A, Narayanan T, Huber K (2010) Evaluation of the particle growth of amorphous calcium carbonate in water by means of the Porod Invariant from SAXS. *Langmuir* 26:17405–17412
- Liu C, Shang J, Zachara JM (2011) Multispecies diffusion models: A study of uranyl species diffusion. *Water Resour Res* 47:W12514, doi: 10.1029/2011WR010575
- Lu G, DePaolo DJ, Kang Q, Zhang D (2009) Lattice Boltzmann simulation of snow crystal growth in clouds. *J Geophys Res: Atmospheres* 114:D07305
- Luan HB, Xu H, Chen L, Sun DL, Tao WQ (2010) Numerical illustrations of the coupling between the lattice Boltzmann method and finite-type macro-numerical methods. *Numerical Heat Transfer, Part B: Fundamentals* 57(2):147–171, doi: 10.1080/15421400903579929
- Luan HB, Xu H, Chen L, Sun DL, He YL, Tao WQ (2011) Evaluation of the coupling scheme of FVM and LBM for fluid flows around complex geometries. *Int J Heat Mass Transf* 54:1975–1985
- Luo H, Quintard M, Debenest G, Laouafa F (2012) Properties of a diffuse interface model based on a porous medium theory for solid–liquid dissolution problems. *Comput Geosci* 16:913–932
- Martin D, Dodds K, Butler IB, Ngwenya BT (2013) Carbonate precipitation under pressure for bioengineering in the anaerobic subsurface via denitrification. *Env Sci Technol* 47:8692–8699, doi: 10.1021/es401270q
- Martys NS, Chen H (1996) Simulation of multicomponent fluids in complex three-dimensional geometries by the lattice Boltzmann method. *Phys Rev E* 53:743
- Meakin P, Tartakovsky AM. (2009) Modeling and simulation of pore-scale multiphase fluid flow and reactive transport in fractured and porous media. *Rev Geophys* 47:RG3002, doi: 10.1029/2008RG000263
- Miller W, Succi S, Mansutti D (2001) Lattice Boltzmann model for anisotropic liquid–solid phase transition. *Phys Rev Letters* 86:3578–3581
- Mohamad AA (2011) *Lattice Boltzmann Method - Fundamentals and Engineering Applications with Computer Codes*. Springer-Verlag, London
- Molins S, Trebotich D, Steefel CI, Shen C (2012) An investigation of the effect of pore scale flow on average geochemical reaction rates using direct numerical simulation. *Water Resour Res* 48:W03527, doi:10.1029/2011WR011404
- Molins S, Trebotich D, Yang L, Ajo-Franklin JB, Ligocki TJ, Shen C, Steefel CI (2014) Pore-scale controls on calcite dissolution rates from flow-through laboratory and numerical experiments. *Environ Sci Technol* 48:7453–7460
- Mozley PS, Davis JM (2005) Internal structure and mode of growth of elongate calcite concretions: Evidence for small-scale, microbially induced, chemical heterogeneity in groundwater. *Geol Soc Am Bull* 117:1400–1412
- Nambi IM, Werth CJ, Sanford RA, Valocchi AJ (2003) Pore-Scale Analysis of Anaerobic Halorespiring Bacterial Growth along the Transverse Mixing Zone of an Etched Silicon Pore Network. *Env Sci Technol* 37:5617–5624
- Navarre-Sitchler A, Brantley S (2007) Basalt weathering across scales. *Earth Planet Sci Lett* 261:321–334
- Navarre-Sitchler A, Steefel CI, Yang L, Tomutsa L, Brantley SL (2009) Evolution of porosity and diffusivity associated with chemical weathering of a basalt clast. *J Geophys Res* 114:F02016, doi:10.1029/2008JF001060
- Nemati M, Voordouw G (2003) Modification of porous media permeability, using calcium carbonate produced enzymatically in situ. *Enzyme Microbiol Technol* 33: 635–642
- Noguera DP, Pizarro G, Stahl DA, Rittmann BE (1999) Simulation of multispecies biofilm development in three dimensions. *Water Sci Technol* 39:123–130

- Ogino T, Suzuki T, Sawada K (1987) The formation and transformation mechanism of calcium carbonate in water. *Geochim Cosmochim Acta* 51:2757–2767
- Oostrom M, Mehmani Y, Romero-Gomez P, Tang Y, Liu H, Yoon H, Kang Q et al. (2014) Pore-scale and continuum simulations of solute transport micromodel benchmark experiments. *Comput Geosci*, doi: 10.1007/s10596-014-9424-0
- Pan C, Luo LS, Miller CT (2006) An evaluation of lattice Boltzmann schemes for porous medium flow simulation. *Comput Fluids* 35:898–909
- Parkhurst DL, Appelo CAJ (2013) Description of input and examples for PHREEQC Version 3—A computer program for speciation, batch-reaction, one-dimensional transport, and inverse geochemical calculations. U.S. Geological Survey Techniques and Methods, Book 6, <http://pubs.usgs.gov/tm/06/a43>
- Parmigiani A, Huber C, Bachmann O, Chopard B (2011) Pore scale mass and reactant transport in multiphase porous media flows. *J Fluid Mech* 686:40–76
- Patel RA, Perko J, Jacques D, De Schutter G, Van Breugel K, Ye G (2014) A versatile pore-scale multicomponent reactive transport approach based on lattice Boltzmann method: Application to portlandite dissolution. *Phys Chem Earth, Parts A/B/C* 70:127–137
- Peters C (2009) Accessibilities of reactive minerals in consolidated sedimentary rock: an imaging study of three sandstones. *Chem Geol* 265:198–208
- Picioreanu C, van Loosdrecht MCM, Heijnen JJ (1998) Mathematical modeling of biofilm structure with a hybrid differential-discrete cellular automaton approach. *Biotechnol Bioeng* 58:101–116
- Picioreanu C, Van Loosdrecht MCM, Heijnen JJ (2000) Effect of diffusive and convective substrate transport on biofilm structure formation: A two-dimensional modeling study. *Biotechnol Bioeng* 69:504–515
- Picioreanu C, van Loosdrecht MCM, Heijnen JJ (2001) Two-dimensional model of biofilm detachment caused by internal stress from liquid flow. *Biotechnol Bioeng* 72:205–218
- Picioreanu C, Kreft JU, van Loosdrecht MCM (2004) Particle-based multidimensional multispecies biofilm model. *Appl Environ Microbiol* 70:3024–3040
- Pintelon TRR, von der Schulenburg DAG, Johns ML (2009) Towards Optimum Permeability Reduction in Porous Media Using Biofilm Growth Simulations. *Biotechnol Bioeng* 103:767–779
- Pintelon TRR, Picioreanu C, van Loosdrecht MCM, Johns ML (2012) The effect of biofilm permeability on bio-clogging of porous media. *Biotechnol Bioeng* 109:1031–1042
- Pouget EM, Bomans PHH, Goos J, Frederik PM, de With G, Sommerdijk N (2009) The initial stages of template-controlled CaCO₃ formation revealed by cryo-TEM. *Science* 323:1455–1458
- Prieto M, Cubillas P, Fernández-Gonzalez Á (2003) Uptake of dissolved Cd by biogenic and abiogenic aragonite: a comparison with sorption onto calcite. *Geochim Cosmochim Acta* 67:3859–3869
- Qian YH, Orszag SA (1995) Scalings in diffusion-driven reaction $A + B \rightarrow C$: Numerical simulations by lattice BGK models. *J Stat Phys* 81:237–253
- Qu WL, Li DQ (2000) A model for overlapped EDL fields. *J Colloid Interfac Sci* 224: 397–407
- Raouf A (2011) Reactive/adsorptive transport in (partially-) saturated porous media; from pore scale to core scale. PhD Dissertation, Utrecht University, Utrecht, Netherlands
- Rieger J, Frechen T, Cox G, Heckmann W, Schmidt C, Thieme J (2007) Precursor structures in the crystallization/precipitation processes of CaCO₃ and control of particle formation by polyelectrolytes. *Faraday Discussions* 136:265–277, doi: 10.1039/B701450C
- Rittmann BE (1993) The significance of biofilms in porous media. *Water Resour Res* 29:2195–2208
- Rittmann BE, McCarty PL (2001) *Environmental Biotechnology*. McGraw-Hill, Boston
- Scheibe TD, Fang Y, Murray CJ, Roden EE, Chen J, Chien YJ, Brooks SC, Hubbard SS (2006) Transport and biogeochemical reaction of metals in a physically and chemically heterogeneous aquifer. *Geosphere* 2:220–235
- Scheibe TD, Murphy EM, Chen X, Rice AK, Carroll KC, Palmer BJ, Tartakovsky AM, Battiato I, Wood BD (2015) An analysis platform for multiscale hydrogeologic modeling with emphasis on hybrid multiscale methods. *Groundwater* 53:38–56
- Seifert D, Engesgaard P (2007) Use of tracer tests to investigate changes in flow and transport properties due to bioclogging of porous media. *J Contam Hydrol* 93:58–71
- Seifert D, Engesgaard P (2012) Sand box experiments with bioclogging of porous media: Hydraulic conductivity reductions. *J Contam Hydrol* 136–137:1–9
- Shan X, Chen H (1993) Lattice Boltzmann model for simulating flows with multiple phases and components. *Phys Rev E* 47:1815
- Shi Y, Zhao TS, Guo ZL (2008) Lattice Boltzmann simulation of thermal electro-osmotic flows in micro/nanochannels. *J Comput Theor Nanosci* 5:236–246
- Smith NS, Notte JA, Steele AV (2014) Advances in source technology for focused ion beam instruments. *MRS Bulletin* 39:329–335, doi:10.1557/mrs.2014.53
- Spanne P, Thovert JF, Jacquin CJ, Lindquist WB, Jones KW, Adler PM (1994) Synchrotron computed microtomography of porous media: topology and transports. *Phys Rev Letters* 73:2001

- Steeffel CI, Lasaga AC (1990) The evolution of dissolution patterns: Permeability change due to coupled flow and reaction. *In: Chemical Modeling of Aqueous Systems II*. Melchior D and Bassett RL (eds) ACS Symposium Series No. 416, American Chemical Society, Washington, p 212–225
- Steeffel CI, Lasaga AC (1994) A coupled model for transport of multiple chemical species and kinetic precipitation/dissolution reactions with application to reactive flow in single phase hydrothermal systems. *Am J Sci* 294:529–592
- Steeffel CI, Lichtner PC (1994) Diffusion and reaction in rock matrix bordering a hyperalkaline fluid-filled fracture. *Geochim Cosmochim Acta* 58:3595–3612
- Steeffel C, Lichtner P (1998) Multicomponent reactive transport in discrete fractures: II: Infiltration of hyperalkaline groundwater at Maqarin, Jordan, a natural analogue site. *J Hydrol* 209:200–224
- Steeffel CI, Molins S, Trebotich D (2013) Pore scale processes associated with subsurface CO₂ injection and sequestration. *Rev Mineral Geochem* 77:259–303
- Stewart TL, Kim DS (2004) Modeling of biomass-plug development and propagation in porous media. *Biochem Eng J* 17:107–119
- Stockman HW, Li C, Wilson JL (1997) A lattice-gas and lattice Boltzmann study of mixing at continuous fracture junctions: Importance of boundary conditions. *Geophys Res Lett* 24:1515–1518
- Succi S (2001) *The Lattice Boltzmann Equation for Fluid Dynamics and Beyond*. Oxford University Press, Oxford
- Sukop M, Thorne DT (2007) *Lattice Boltzmann Modeling: An Introduction for Geoscientists and Engineers*. Springer, 2nd edition, Heidelberg, Berlin, New York
- Sullivan SP, Sani FM, Johns ML, Gladden LF (2005) Simulation of packed bed reactors using lattice Boltzmann methods. *Chem Eng Sci* 60:3405–3418
- Sullivan SP, Gladden LF, Johns ML (2006) 3D chemical reactor LB simulations. *Math Comput Simul* 72:206–211
- Sun D, Zhu M, Pan S, Raabe D (2009) Lattice Boltzmann modeling of dendritic growth in a forced melt convection. *Acta Materialia* 57:1755–1767
- Tang Y, Valocchi AJ (2013) An improved cellular automaton method to model multispecies biofilms. *Water Research* 47:5729–5742
- Tang Y, Valocchi AJ, Werth CJ, Liu H (2013) An improved pore-scale biofilm model and comparison with a microfluidic flow cell experiment. *Water Resour Res* 49:8370–8382
- Tartakovsky AM, Meakin P, Scheibe TD, Wood BD (2007) A smoothed particle hydrodynamics model for reactive transport and mineral precipitation in porous and fractured porous media. *Water Resour Res* 43(5):W05437, doi:10.1029/2005WR004770
- Tartakovsky AM, Redden G, Lichtner PC, Scheibe TD, Meakin P (2008) Mixing-induced precipitation: Experimental study and multiscale numerical analysis. *Water Resour Res* 44:W06S04
- Tartakovsky AM, Scheibe TD, Meakin P (2009) Pore-scale model for reactive transport and biomass growth. *J Porous Media* 12:417–434
- Taylor SW, Jaffé PR (1990) Biofilm growth and the related changes in the physical properties of a porous medium: 1. Experimental investigation. *Water Resour Res* 26:2153–2159
- Thullner M, Baveye P (2008) Computational pore network modeling of the influence of biofilm permeability on bioclogging in porous media. *Biotechnol Bioeng* 99:1337–1351
- Tomin P, Lunati I (2013) Hybrid Multiscale Finite Volume method for two-phase flow in porous media. *J Comput Phys* 250: 293–307
- Tong ZX, He YL (2015) A unified coupling scheme between lattice Boltzmann method and finite volume method for unsteady fluid flow and heat transfer. *Int J Heat Mass Transf* 80:812–824
- Valocchi AJ (2012) Hydrogeochemical models. *In: Delivery and Mixing in the Subsurface: Processes and Design Principles for In Situ Remediation*. Kitanidis PK, McCarty PL (eds) Springer, New York, p 77–116
- Van Cappellen P, Gaillard JF (1996) Biogeochemical dynamics in aquatic sediments. *Rev Mineral* 34:335–376
- Vandevivere P, Baveye P (1992) Saturated hydraulic conductivity reduction caused by aerobic bacteria in sand columns. *Soil Sci Soc Amer J* 56:1–13
- Varloteaux C, Bécri S, Adler PM (2013) Pore network modelling to determine the transport properties in presence of a reactive fluid: From pore to reservoir scale. *Adv Water Resour* 53:87–100
- Verberg R, Ladd AJC (2000). Lattice-Boltzmann model with sub-grid-scale boundary conditions. *Phys Rev letters* 84:2148
- Verberg R, Ladd AJC (2002) Simulation of chemical erosion in rough fractures. *Phys Rev E* 65:056311
- Verhaeghe F, Arnout S, Blanpain B, Wollants P (2006) Lattice-Boltzmann modeling of dissolution phenomena. *Phys Rev E* 73:036316
- Vilcáez J, Li L, Wu D, Hubbard SS (2013) Reactive transport modeling of induced selective plugging by *Leuconostoc mesenteroides* in carbonate formations. *Geomicrobiol J* 30:813–828
- von der Schulenburg DAG, Pintelon TRR, Picioreanu C, Van Loosdrecht MCM, Johns ML (2009) Three-dimensional simulations of biofilm growth in porous media. *AIChE J* 55:494–504

- Wang MR, Kang QJ (2009) Electrokinetic transport in microchannels with random roughness. *Anal Chem* 81:2953–2961
- Wang MR, Kang QJ (2010) Modeling electrokinetic flows in microchannels using coupled lattice Boltzmann methods. *J Comput Phys* 229:728–744
- Wang Q, Zhang T (2010) Review of mathematical models for biofilms. *Solid Stat Comm* 150:1009–1022
- Wang JK, Wang M, Li ZX (2006) Lattice Poisson-Boltzmann simulations of electro-osmotic flows in microchannels. *J Colloid Interfac Sci* 296:729–736
- Wang D, Summers JL, Gaskell PH (2008) Modelling of electrokinetically driven mixing flow in microchannels with patterned blocks. *Comput Math Appl* 55:1601–1610
- Wang M, Kang QJ, Ben-Naim E (2010a) Modeling of electrokinetic transport in silica nanofluidic channels. *Anal Chimica Acta* 664:158–164
- Wang M, Kang QJ, Viswanathan H, Robinson BA (2010b) Modeling of electro-osmosis of dilute electrolyte solutions in silica microporous media. *J Geophys Res* 115:B10205, doi:10.1029/2010JB007460
- Weimar JR, Boon JP (1996) Nonlinear reactions advected by a flow. *Physica A* 224:207–215
- Weinan E, Engquist B, Li X, Ren W, Vanden-Eijnden E (2007). Heterogeneous multiscale methods: a review. *Commun Comput Phys* 2:367–450
- Wells JT, Janecky DR, Travis BJ (1991) A lattice gas automata model for heterogeneous chemical reactions at mineral surfaces and in pore networks. *Physica D* 47:115–123
- Wildenschild D, Sheppard AP (2013) X-ray imaging and analysis techniques for quantifying pore-scale structure and processes in subsurface porous medium systems. *Adv Water Resour* 51: 217–46
- Wolf-Gladrow D (2000) Lattice-Gas Cellular Automata and Lattice Boltzmann Models - An Introduction. Springer, Verlag
- Xu Z, Meakin P, Tartakovsky A, Scheibe T (2011) Dissipative-particle-dynamics model of biofilm growth. *Phys Rev E* 83:066702
- Yan GW, Yuan L (2001) A lattice Boltzmann method for the chemical clock in the Belousov-Zhabotinskii reaction. *Chin Phys Lett* 18:918–920
- Yang RJ, Fu LM, Hwang CC (2001) Electroosmotic entry flow in a microchannel. *J Colloid Interfac Sci* 244:173–179
- Yang X, Liu C, Shang J, Fang Y, Bailey VL (2014a) A Unified multiscale model for pore-scale flow simulations in soils. *Soil Sci Soc Am J* 78:108–118
- Yang X, Shi B, Chai Z, Guo Z (2014b) A Coupled Lattice Boltzmann Method to Solve Nernst-Planck Model for Simulating Electro-osmotic Flows. *J Sci Comput* 61:222–238
- Yoon H, Valocchi AJ, Werth CJ, Dewers T (2012) Pore-scale simulation of mixing-induced calcium carbonate precipitation and dissolution in a microfluidic pore network. *Water Resour Res* 48:W02524
- Yoon H, Dewers T (2013) Nanopore structures, statistically representative elementary volumes, and transport properties of chalk. *Geophys Res Lett* 40:4294–4298
- Yoon H, Leibel S, Zhang C, Müller RH, Werth CJ, Zilles JL (2014) Adaptation of *Delftia acidovorans* for degradation of 2,4-dichlorophenoxyacetate in a microfluidic porous medium. *Biodegradation* 25:595–604
- Yu D, Ladd AJC (2010) A numerical simulation method for dissolution in porous and fractured media. *J Comput Phys* 229:6450–6465
- Yu D, Mei R, Luo L, Shyy W (2003) Viscous flow computations with the method of lattice Boltzmann equation. *Prog Aerosp Sci* 39:329–367
- Zarghami A, Maghrebi MJ, Ghasemi J, Ubertini S (2012) Lattice Boltzmann finite volume formulation with improved stability. *Comm Comput Phys* 12:42
- Zhang J (2011) Lattice Boltzmann method for microfluidics: models and applications. *Microfluid Nanofluid* 10:1–28
- Zhang T, Klapper I (2014) Critical occlusion via biofilm induced calcite precipitation in porous media. *New J Phys* 16:055009
- Zhang C, Dehoff K, Hess N, Ostrom M, Wietsma TW, Valocchi AJ, Fouke BW, Werth CJ (2010a) Pore-scale study of transverse mixing induced CaCO₃ precipitation and permeability reduction in a model subsurface sedimentary system. *Environ Sci Technol* 44:7833–7838
- Zhang C, Kang Q, Wang X, Zilles JL, Müller RH, Werth CJ (2010b) Effects of pore-scale heterogeneity and transverse mixing on bacterial growth in porous media. *Environ Sci Technol* 44:3085–3092, doi: 10.1021/es903396h
- Zhang T, Shi B, Guo Z, Chai Z, Lu J (2012) General bounce-back scheme for concentration boundary condition in the lattice-Boltzmann method. *Phys Rev E* 85:016701
- Zhu H, Carlson HK, Coates JD (2013) Applicability of anaerobic nitrate-dependent Fe(II) oxidation to microbial enhanced oil recovery (MEOR). *Environ Sci Technol* 47(15):8970-7, doi: 10.1021/es401838b